Turbulent coagulation of colloidal particles

By BRETT K. BRUNK[1], DONALD L. KOCH[1]†
AND LEONARD W. LION[2]

[1] School of Chemical Engineering, Cornell University, Ithaca, NY 14853, USA
[2] School of Civil and Environmental Engineering, Cornell University, Ithaca, NY 14853, USA

Theoretical predictions for the coagulation rate induced by turbulent shear have often been based on the hypothesis that the turbulent velocity gradient is persistent (Saffman & Turner 1956) and that hydrodynamic and interparticle interactions (van der Waals attraction and electrostatic double-layer repulsion) between colloidal particles can be neglected. In the present work we consider the effects of interparticle forces on the turbulent coagulation rate, and we explore the response of the coagulation rate to changes in the Lagrangian velocity gradient correlation time (i.e. the characteristic evolution time for the velocity gradient in a reference frame following the fluid motion). Stokes equations of motion apply to the relative motion of the particles whose radii are much smaller than the lengthscales of turbulence (i.e. small particle Reynolds numbers). We express the fluid motion in the vicinity of a pair of particles as a locally linear flow with a temporally varying velocity gradient. The fluctuating velocity gradient is assumed to be isotropic and Gaussian with statistics taken from published direct numerical simulations of turbulence (DNS). Numerical calculations of particle trajectories are used to determine the rate of turbulent coagulation in the presence and absence of particle interactions. Results from the numerical simulations correctly reproduce calculated coagulation rates for the asymptotic limits of small and large total strain where total strain is a term used to describe the product of the characteristic strain rate and its correlation time. Recent DNS indicate that the correlation times for the fluctuating strain and rotation rate are of the same order as the Kolmogorov time (Pope 1990), suggesting theories that assume either small or large total strain may poorly approximate the turbulent coagulation rate. Indeed, simulations for isotropic random flows with intermediate total strain indicate that the coagulation rate in turbulence is significantly different from the analytical limits for large and small total strain. The turbulent coagulation rate constant for non-interacting monodisperse particles scaled with the Kolmogorov time and the particle radius is 8.62 ± 0.02, whereas the commonly used model of Saffman & Turner (1956) predicts a value of 10.35 for non-rotational flows in the limit of persistent turbulent velocity gradients. Additional simulations incorporating hydrodynamic interactions and van der Waals attraction were used to estimate the actual rate of particle coagulation. For typical values of these parameters, particle interactions reduced the coagulation rate constant by at least 50%. In general, the collision efficiency (the ratio of coagulation with particle interactions to that without) decreased with increasing particle size and Kolmogorov shear rate.

---

† Author to whom correspondence should be addressed: 120 Olin Hall, Cornell University, Ithaca, NY 14853, 607-255-3484, USA; e-mail: don@cheme.cornell. edu.

1. Introduction

Turbulent-shear-induced coagulation is an important process leading to the aggregation of colloidal particles in both engineered and environmental processes. Turbulent mixing is heavily employed in water treatment and the chemical industries to enhance the aggregation and removal of fine particles. In natural aquatic systems many pollutants associate strongly with particles and therefore considerable effort has been focused on understanding the dynamics of particles in natural environments (O'Melia 1980).

Estuaries serve as an excellent example of natural systems in which particle aggregation, due to turbulence, controls contaminant transport. Polluted suspended sediment in river water mixes with sea water in the estuary resulting in destabilization and the subsequent aggregation of colloidal particles. Large contaminated agglomerates form which can readily settle through the water column and deposit onto the estuarine sediments (Stumm & Morgan 1981).

Given typical estuarine conditions, with turbulent dissipation rates ranging from 0.002 to 0.7 cm² s⁻³ (Krone 1970) and colloidal particles with radii between 0.5 and 10 μm and a density of 20 g cm⁻³ (McCave 1984), scaling analysis incorporating coagulation rate constants summarized by Pearson, Valioulis & List (1984) can be used to ascertain the relative importance of various coagulation mechanisms. For 5 μm particles, coagulation rates resulting from Brownian motion are estimated to be 10–2000 times slower than turbulent shear coagulation for turbulent energy dissipation rates between 0.002 and 0.7 cm² s⁻³. Turbulent coagulation also dominates over differential-settling-induced coagulation in which 5 μm particles aggregate with particles ranging from 4 to 6 μm at low turbulence levels and from 3 to 8 μm particles at high turbulence levels. Turbulent acceleration can increase the coagulation rate of particles owing to differences in particle inertia. From the work of Saffman & Turner (1956), the ratio of coagulation due to shear and particle inertia in a turbulent flow can be calculated as a function of the particle relaxation time (i.e. the time it takes an initially stationary particle to accelerate to the fluid velocity), the relative density difference between the bulk fluid and the particle and the turbulent dissipation rate. Again, using the parameter estimates typical for estuarine conditions, turbulent shear coagulation is expected to dominate for similarly sized particles. At low turbulence levels, the transition from turbulent shear to inertia dominated collisions occurs for 5 μm particles interacting with particles less than 4 μm and greater than 6 μm. Since the importance of particle inertia decreases with the density difference between the particle and the fluid, inertia driven coagulation is expected to be less important for more neutrally buoyant, organic-based colloidal particles. In general, this scaling analysis suggests that coagulation caused by turbulent shear is likely to control the aggregation process in estuaries for like-sized colloids with radii greater than 1 μm.

Despite the importance of turbulent coagulation, only a limited number of theoretical analyses have been attempted and very little experimental work has been carried out to assess the applicability of existing turbulent coagulation models. In this paper the issue of analytical model validity is addressed by performing computer simulations of turbulent shear coagulation. The relative trajectories of particle pairs in isotropic turbulence are analysed using velocity gradient statistics taken from direct numerical simulations of turbulence (DNS; Girimaji & Pope 1990). Results from the simulations are compared with models for turbulent coagulation that are found in the literature (i.e. Saffman & Turner 1956; Brunk, Koch & Lion 1997).

Although several heuristic models for turbulent coagulation have been proposed
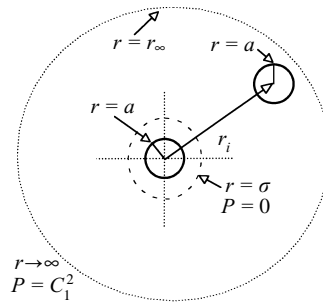
FIGURE 1. Schematic illustrating the coordinate system and boundary conditions for turbulent coagulation. Two particles with radii a are separated by a distance r. Far from the test sphere, $r \to r_\infty$ the pair probability for the particles reaches its bulk value, C_1^2 and upon reaching the collision radius, $r = \sigma = 2a$ the pair probability of singlet particles is zero.

(Delichatsios & Probstein 1975; Camp & Stein 1943; Casson & Lawler 1990), the discussion presented here will focus on models that attempt to represent the physics of turbulent coagulation. The model developed by Saffman & Turner (1956) yields an expression for the turbulent aggregation rate that is valid in the limit of persistent strain where the product of the characteristic strain rate and its correlation time (i.e. the total strain) is large. We have recently investigated the opposite limit where turbulent transport of coagulating particles can be likened to a pair diffusion process (Brunk *et al.* 1997). Evidence from DNS (Pope 1990; Girimaji & Pope 1990) suggests that the strain rate field for isotropic turbulence is intermediate between these two limits. In the intermediate regime, analytical expressions for the turbulent coagulation rate are unattainable; thus, we simulate numerically the coagulation of particles that are smaller than the lengthscales of turbulence.

For the analysis that follows, particle diameters are assumed to be smaller than the Kolmogorov lengthscale (i.e. the lengthscale of the smallest turbulent eddies), but large enough that the Péclet number based on the small scales of turbulence is large and Brownian motion can be ignored.

Since the smallest scales of turbulence have the highest shear rates (Tennekes & Lumley 1972), they will dominate the coagulation process. The size and shear rate of the smallest turbulent eddies are estimated by balancing the turbulent energy flux from large to small eddies with viscous dissipation. Characterizing the energy flux with the turbulent dissipation rate, ϵ, and the viscous dissipation with the kinematic viscosity, ν, leads to the Kolmogorov estimates for eddy length and velocity gradient:

$$\eta = \left(\frac{\nu^3}{\epsilon}\right)^{1/4}, \qquad (1.1)$$

$$\Gamma_\eta = \left(\frac{\epsilon}{\nu}\right)^{1/2}, \qquad (1.2)$$

where η is the Kolmogorov lengthscale and Γ_η is the Kolmogorov velocity gradient.

In natural aquatic environments, such as an estuary, typical Kolmogorov lengthscales vary from 1.5 mm to 350 μm (Krone 1970), while turbulence produced in flocculation tanks used for wastewater treatment might have Kolmogorov lengths as small as 30 μm (O'Melia 1980). The stipulation that the particles be smaller than the lengthscales of turbulence is, therefore, applicable to all but the most intense turbulent flows and the largest colloidal particles.

Figure 1 shows the standard coagulation problem where calculation of the collision rate between monodisperse particles is of interest. The coordinate system is placed in a Lagrangian reference frame that moves with a test particle and relative position vectors connect the centre of the test sphere and nearby particles. In this description, the system is assumed to be sufficiently dilute such that only binary (1:1) interactions occur. The coagulation rate is obtained by calculating the number of two-particle collisions that occur between the representative test particle at the origin of the coordinate system and other colloids. Doublet formation is assumed to be irreversible so that the probability density for pairs of free particles (P) approaches zero at the excluded volume surface: $r = \sigma = 2a$. At large distances from the test sphere ($r \rightarrow \infty$), the pair probability of monodisperse particles attains its bulk value, $P = C_1^2$, where C_1 is the bulk concentration of singlet particles in the system.

Given the assumption of negligible doublet breakup, the initial rate of doublet formation in a dilute suspension is:

$$\frac{dC_2}{dt} = kC_1^2, \tag{1.3}$$

where k is the coagulation kernel or coagulation rate constant and C_2 is the bulk concentration of doublet particles.

The coagulation kernel, k, given in (1.3), accounts for the various transport mechanisms leading to particle collision (e.g. turbulent shear, Brownian motion and differential settling), and the influence of interparticle interactions such as van der Waals attraction, hydrodynamic interactions and electrostatic double-layer repulsion. Transport mechanisms and interparticle interactions are usually separated by writing the coagulation kernel as the quotient of an ideal rate constant, k^0, that ignores interparticle forces and hydrodynamic interactions and a stability factor, W, that incorporates the effects of these interactions (Russel, Saville & Schowalter 1989). Equivalently, the rate constant can be described in terms of a collision efficiency, $\alpha = W^{-1}$, expressing the fraction of ideal collisions that actually would occur when interparticle interactions are included. Thus coagulation for monodisperse spherical particles undergoing irreversible collisions can be represented by:

$$\frac{dC_2}{dt} = \alpha k^0 C_1^2. \tag{1.4}$$

The rate expression given by (1.4) assumes there are no particle sources in the system. A consequence of the assumption that the suspension is dilute is that C_2 and C_1 are independent of position on lengthscales greater than the particle radius. That is, the time between collisions is much longer than the local mixing time so that local fluctuations in the bulk particle concentration can be neglected. We can estimate how dilute the suspension must be to ignore concentration fluctuations by comparing the characteristic mixing time to the time over which the particle number density evolves. The number density evolves on a timescale, $\tau_c \sim 1/k^0 C_1$. For particles which are small compared to the lengthscales of turbulence, dimensional analysis shows that $k^0 \sim \sigma^3 \Gamma_\eta$, where σ is the particle diameter. Thus, $\tau_c \sim 1/\Gamma_\eta \phi$ where ϕ is the particle volume fraction. The time to mix over a Kolmogorov lengthscale is $\ln(\eta/\sigma)/\Gamma_\eta$ if we let the relative velocity between the two particles be proportional to $\Gamma_\eta r$, where r is the relative separation vector between the particles. Mixing at the macroscales of turbulence occurs over times of the order of L/u' where L is the integral scale of the turbulence and u' is the integral velocity. The ratio of the Kolmogorov scale to integral scale mixing rates

is proportional to $R^{1/2}\ln(\eta/\sigma)$ where R is the turbulent Reynolds number (Tennekes & Lumley 1972). For all practical purposes, mixing at the large scales is rate limiting. Comparing the characteristic coagulation timescale, τ_c to the mixing time at the macroscales of turbulence gives the criterion: $\phi \quad R^{-1/2}$ for the rapid mixing assumption to be valid. In natural environments, volume fractions are of the order of 10^{-5} or smaller (Stumm & Morgan 1981); thus, neglecting local concentration fluctuations should be valid for many practical systems. If the suspension is sufficiently concentrated so that mixing limitations on the larger scales are important, the average coagulation rate can be written as:

$$\frac{\mathrm{d}C_2}{\mathrm{d}t} = \langle \alpha k^0 C_1^2 \rangle, \tag{1.5}$$

where the brackets indicate an average over the larger eddies with lengthscales much larger than η. Here C_1 and C_2 would be interpreted as concentrations averaged over a lengthscale which is large compared to the particle radius, but small compared to the large eddies. In this situation, we would need a model for the macroscale mixing process so the nonlinear average in (1.5) could be evaluated. For the remainder of this paper we assume a well-mixed system.

Asymptotic expressions for k^0 in turbulence have been obtained in the large and small total strain limits. Assuming the product of the characteristic strain rate and its correlation time are large, Saffman & Turner (1956) derive the coagulation rate constant of non-interacting particles in stationary, homogeneous, isotropic turbulence. In the neighbourhood of a test particle, they propose that the local turbulent velocity field can be represented as a pseudosteady linear extensional flow. The particle collision rate is written as a flux integral over the excluded volume surface area that is simplified by assuming isotropic and Gaussian velocity gradient statistics. The resulting average coagulation rate constant in the large strain limit is:

$$k^0 = (\tfrac{8}{15}\pi)^{1/2} \Gamma_\eta \sigma^3. \tag{1.6}$$

In recent work, the authors extend the analysis of Levich (1962) and calculate the coagulation rate in the limit of small strain with and without particle interactions (Brunk *et al.* 1997). At small total strain, net particle movement is the result of many uncorrelated velocity field fluctuations; therefore, relative particle movement can be characterized with a pair diffusivity. This analysis is restricted to small gap widths where the flow field is a randomly varying isotropic linear flow with Gaussian statistics and separate rotational and extensional correlation times. Neglecting hydrodynamic interactions, the pair diffusivity is:

$$D_{ij}^t = \frac{\Gamma_\eta r^2}{60} \left[4\Gamma_\eta \tau_S \frac{r_i r_j}{r^2} + (3\Gamma_\eta \tau_S + 5\Gamma_\eta \tau_R)\left(\delta_{ij} - \frac{r_i r_j}{r^2}\right) \right], \tag{1.7}$$

where r_i is the vector connecting the centres of the diffusing particle pair, r is the magnitude of r_i, δ_{ij} is the identity tensor and τ_S and τ_R are the strain and rotation rate correlation times, respectively.

The turbulent coagulation rate constant is found by solving a steady-state pair probability equation for the flux of particles diffusing toward a test sphere (Brunk *et al.* 1997). In the absence of particle interactions:

$$k^0 = \tfrac{4}{5}\pi(\Gamma_\eta \tau_S) \Gamma_\eta \sigma^3. \tag{1.8}$$

This prediction has a functional form similar to the large strain limit determined by Saffman & Turner (1.6) except for the additional dependence on the total strain, $\Gamma_\eta \tau_S$.

It can be further shown that the effects of finite Péclet number, hydrodynamic interactions, and interparticle forces may be easily included in numerical computations at the small strain limit (Brunk *et al.* 1997).

Evidence from DNS suggests that the total strain in isotropic turbulence is order one. Using DNS, Pope and coworkers (Pope 1990; Girimaji & Pope 1990; Yeung & Pope 1989) investigated one-point, two-time Lagrangian autocorrelation functions of the strain and rotation rates in homogeneous, isotropic turbulence over Taylor-scale Reynolds numbers from 38 to 93. [NB By one-point, two-time Lagrangian strain rate autocorrelation function we mean the covariance of the strain rate at two different times for the same fluid element. The Taylor-scale Reynolds number is defined as $R_\lambda = u'\lambda_T/\nu \approx R^{1/2}$, where $\lambda_T = ((u')^2/\langle(\partial u_1/\partial x_1)^2\rangle)^{1/2}$ is the Taylor scale and u_1 is the velocity in the x_1-direction.] At all Reynolds numbers, Pope (1990) found that, whereas the correlation time for the amplitude of the Lagrangian strain rate scales with the integral timescale, the strain rate loses directional information in approximately a Kolmogorov time. This result contradicts the long-standing hypothesis of persistent strain in turbulence. According to the persistent strain hypothesis (Townsend 1951; Pope 1990), the local Lagrangian strain rate scales with the integral timescale. In the context of particle aggregation, this hypothesis forms the basis of Saffman & Turner's (1956) analysis and is equivalent to assuming the flow field remains static over a collision event. Based on the DNS results, it is reasonable to expect that neither the large nor small total strain asymptotic limits will adequately represent coagulation in isotropic turbulence. Estimates of the turbulent coagulation rate at moderate strain and rotation rate correlation times must be determined by simulations before the regions of validity for the asymptotes can be established. In addition, these calculations can provide insight into aggregation phenomena in other random flows such as the flow in porous media.

Recently, several studies have been undertaken into the collisions among particles in DNS generated isotropic turbulent flows (Sundaram & Collins 1997; Wang, Wexler & Zhou 1998; Zhou, Wexler & Wang 1998). Wang *et al.* (1998) investigated collisions of inertialess particles. Sundaram & Collins (1997) and Zhou *et al.* (1998) considered particles with appreciable inertia, i.e. heavy particles suspended in a gas. In the presence of appreciable particle inertia, the collision rate was found to be much larger than rates occurring in the inertialess case relevant to liquid–solid suspensions. Owing to computational limitations, these simulations omitted interparticle interactions.

DNS has also revealed that inertia causes particles whose density is greater than that of the fluid to accumulate in regions of high local strain and low vorticity (Squires & Eaton 1991; Wang & Maxey 1993; Sundaram & Collins 1997). The extent of preferential accumulation depends on the value of the Stokes number (*St*) based upon the Kolmogorov scale, which is a ratio of the particle response time, ($2\rho a^2/9\mu$, where ρ is the particle density and μ is the fluid viscosity) to the Kolmogorov timescale ($1/\Gamma_\eta$) (Sundaram & Collins 1997). Segregation due to inertia is important at intermediate values of *St*, whereas at large Stokes numbers the particles are so heavy they are unresponsive to the turbulent flow field. When $St \to 0$ the particles have no inertia and they follow the fluid motion and are fully mixed (Squires & Eaton 1991).

The calculations of Squires & Eaton (1991) and Sundaram & Collins (1997) are primarily concerned with solid particles suspended in air where Stokes numbers are large. In contrast, this research focuses on computing the coagulation rate for aqueous colloidal suspensions with no appreciable buoyancy. Only recently have attempts been made to use DNS to simulate coagulation in the limit of low particle inertia (Zhou *et al.* 1998). Zhou *et al.* simulated particle coagulation in frozen turbulence that was

generated with a DNS scheme. Their results suggest the Stokes number based on the Kolmogorov timescale must be less than 0.1 for the collision kernel to be within 10% of the zero inertia value. Assuming neutrally buoyant particles with a diameter 10% of η, $St_\eta < 0.01$ suggesting that particle inertia can be neglected and the particles can be assumed to be distributed homogeneously throughout the turbulent flow. In the conclusions to this manuscript we compare these DNS studies to our own investigations.

In the remainder of the paper, we investigate aggregation in turbulent flows for colloidal particles. In §2, a simulation technique is developed to compute the coagulation rate for arbitrary strain and rotation rate correlation time. We report on simulations conducted without the presence of particle interactions for arbitrary total strain in §3, and compare results for strain rates of practical interest with the commonly used asymptotic limits. Finally, in §4 we include the influence of hydrodynamic interactions and van der Waals attractions in the coagulation simulations. The collision efficiency is computed and the effect of varying the total strain and the relative magnitude of the van der Waals attraction and the viscous interaction force is examined.

2. Computer simulation: development and method

To evaluate the usefulness of the large and small strain limiting cases, we developed a computer simulation of coagulation in a randomly varying flow field with statistics selected to reproduce those for Gaussian isotropic turbulence. The evolution equation for the relative motion of a pair of particles in isotropic turbulence is derived here and the constitutive relations for the fluctuating velocity gradient and interparticle potential are presented. In the forthcoming analysis, the particle-separation-based Reynolds number, $Re = Ur/\nu$ (where U is the relative particle velocity and ν is the kinematic viscosity), is assumed to be small so that Stokes equations apply to the relative particle motion. In addition, we assume the particle suspension is dilute so that the particles do not influence the turbulent flow (Sundaram & Collins 1997). Coagulation is controlled by particle relative motions at small separations where the velocity field is linear in the separation distance. We show how the fluctuating velocity gradient can be described in terms of a Fourier series with coefficients and frequencies chosen randomly to satisfy the constraints of Gaussian isotropic turbulence. The effects of retarded van der Waals attraction and hydrodynamic interactions are also considered in the algorithm. Generalization to other spherically symmetric interparticle potentials can be made in a similar manner.

Neglecting inertia, the evolution of the relative particle separation can be described as a superposition of the motion driven by the linear flow field and the velocity caused by a radially acting interparticle potential:

$$\frac{\mathrm{d}r_i}{\mathrm{d}t} = \Gamma_{ik}(t)r_k - C_{ij}S_{jk}r_k - \left(\frac{M_{ij}}{6\pi\mu a}\right)\frac{\partial\phi(r)}{\partial r_j}, \tag{2.1}$$

where $\Gamma_{ik}(t)$ is randomly fluctuating velocity gradient tensor, $C_{ij}(r)$ is the hydrodynamic mobility function for two particles in a linear flow field (Batchelor & Green 1972a, b), $S_{jk} = \frac{1}{2}(\Gamma_{jk} + \Gamma_{kj})$ is the strain rate, $M_{ij}(r)/6\pi\mu a$ is the relevant hydrodynamic mobility function for two particles experiencing equal and opposite forces (Batchelor 1976) and $\phi(r)$ is the radially acting interparticle potential. The magnitude of the fluctuating velocity gradient is assumed to be large compared with the mean shear so only the

fluctuating motions are dynamically important in determining particle movement and coagulation. Our assumption applies to most flows since the ratio of the mean shear rate to the Kolmogorov shear rate typically scales like $R^{-1/2}$ (Tennekes & Lumley 1972).

Batchelor & Green (1972 a, b) provide an explicit tensor expression for C_{ij} in terms of the particle separation vector and two scalar functions of the relative position and particle radius ratio, namely:

$$C_{ij} = A(r)\frac{r_i r_j}{r^2} + B(r)\left(\delta_{ij} - \frac{r_i r_j}{r^2}\right), \qquad (2.2)$$

where $A(r)$ and $B(r)$ are non-dimensional functions of radial position and radius ratio that are tabulated by Batchelor & Green (1972 a, b) and Kim & Karilla (1991). The hydrodynamic relative mobility tensor scaled with the Stokes drag has the following form (Batchelor 1976):

$$M_{ij} = \frac{r_i r_j}{r^2}G(r) + \left(\delta_{ij} - \frac{r_i r_j}{r^2}\right)H(r), \qquad (2.3)$$

where $G(r)$ and $H(r)$ are non-dimensional functions of relative position and particle radius ratio that are tabulated in Batchelor (1976) and Kim & Karilla (1991).

2.1. *Characterization of $\Gamma_{ij}(t)$*

The fluctuating velocity gradient tensor, $\Gamma_{ij}(t)$, is a small-scale quantity of turbulence with an energy spectrum that peaks in the dissipation subrange of turbulence. Since directional biases imposed at the large scales are lost during the turbulent energy cascade process, Kolmogorov's similarity hypothesis applies and $\Gamma_{ik}(t)$ may be assumed to be isotropic. For the following analysis, we approximate the probability distribution function (p.d.f.) of $\Gamma_{ik}(t)$ as Gaussian. It is established that rare events attributed to internal intermittency lead to the formation of exponential tails on the velocity derivative p.d.f. (Pope 1996). Since exponential decay is much slower than the tailing of the standard Gaussian distribution, this leads to higher-order moments, such as the superskewness (the sixth moment of the velocity gradient), that are orders of magnitude larger than values predicted from a normal distribution (Pope 1996). However, experimental evidence shows that the exponential tails of the velocity gradient distribution contribute negligibly to lower-order statistics such as second moments.

The analysis of turbulent shear coagulation in the small total strain limits (Saffman & Turner 1956; Brunk *et al.* 1997 a) depends only on the second moment. Wang *et al.* (1998) evaluated the Gaussian flow approximation used in Saffman & Turner's expression (1956) for the coagulation rate with DNS at a Taylor microscale Reynolds number of 24. They found the assumption of Gaussian turbulence increased the predicted aggregation rate by about 5 % (Wang *et al.* 1998). Since intermittency has a negligible effect in the two asymptotic limits, it is anticipated that the effects of intermittency will not strongly influence turbulent coagulation at intermediate total strains. The effect of intermittency is likely to be even smaller when we include particle interactions in §4 because the coagulation rate has a much weaker dependence on the Kolmogorov shear rate. It may, however, be expected that the non-Gaussian nature of the flow will become more pronounced with increasing R_λ. The approach developed here could be generalized to allow for a non-Gaussian random velocity gradient field, but this would require knowledge of the temporal correlations of the higher-order moments.

There is one other possible deviation from actual turbulence that our model may exhibit (assuming we accept the local linearity of the flow): actual turbulence may have different types of decay for the velocity gradient correlations. Girimaji & Pope (1990) show that the strain rate tensor and the vorticity vector decay exponentially with correlation times. They found that the ratio of the correlation times with the Kolmogorov time was independent of the Taylor-scale Reynolds number (for simulations from $R_\lambda = 38$ to 93). It is conceivable that there is a weak dependence on R_λ that would become evident if the Reynolds number could be increased substantially, but at present we have no evidence for this. Scalar measures of the dissipation rate and the magnitude of the vorticity do have correlation times that decay on the integral and Kolmogorov times. So the rates of coagulation occurring in different regions of the flow could be different, but this does not change the way we should calculate individual coagulation events that occur on the Kolmogorov scales. The simulations by Pope's group (Pope 1990; Girimaji & Pope 1990; Yeung & Pope 1989) indicate that regions of high strain rate or high vorticity magnitude persist, but the directionality of the strain rate tensor and the vorticity vector change so that the particles' relative motion will not be persistent.

Since a joint-normal distribution is assumed for $\Gamma_{ik}(t)$, only the mean and covariance tensor must be specified to fully define the p.d.f. of $\Gamma_{ik}(t)$. Following the work of Kraichnan (1970), $\Gamma_{ij}(t)$ is written as a temporal Fourier series with random Fourier coefficients and frequencies selected from specified p.d.f.s (see below) to reproduce the two-time Lagrangian statistics of the fluctuating turbulent velocity gradient. As the number of terms in the Fourier series increases, the velocity gradient field automatically becomes Gaussian by the Central Limit Theorem.

The fluctuating velocity gradient is written as a random Fourier series for the rate of strain tensor, $S_{ik}(t)$, and the rotation rate tensor, $R_{ik}(t) = \frac{1}{2}(\Gamma_{ik} - \Gamma_{ki})$. The dependence of $\Gamma_{ik}(t)$ on the strain and rotation rates is made explicit since they evolve according to different timescales (Girimaji & Pope 1990). The Fourier series representation of $\Gamma_{ik}(t)$ is:

$$\Gamma_{ik}(t) = \sum_{n=1}^{N} [\hat{S}_{ik}^n \exp(i\pi\omega_S^n t) + \hat{R}_{ik}^n \exp(i\pi\omega_R^n t)], \tag{2.4}$$

where N is the number of terms in the Fourier series, $i = (-1)^{1/2}$, $\hat{S}_{ik}^n$ and $\hat{R}_{ik}^n$ are independent Gaussian random variables with zero mean that represent the strain and rotation components of the turbulent velocity gradient, respectively, and ω_S^n and ω_R^n are random frequencies chosen from p.d.f.s that reproduce the desired strain and rotation rate autocorrelation functions, respectively.

Expressions for the covariance of the Fourier coefficients and the p.d.f.s of the frequencies are developed below. We explicitly derive relations for the strain rate; the comparable relations involving the rotation rate can be found analogously. Taking the symmetric part of (2.4) yields:

$$S_{ik}(t) = \sum_{n=1}^{N} \hat{S}_{ik}^n \exp(-i\pi\omega_S^n t). \tag{2.5}$$

Multiplying (2.5) by $S_{jl}(t+\tau)$ and taking the ensemble average leads to an expression for the strain rate autocorrelation function:

$$\langle S_{ik}(0) S_{jl}(\tau) \rangle = \left\langle \sum_{n,\,m=1}^{N} \hat{S}_{ik}^n \hat{S}_{jl}^{m*} \exp(i\pi\omega_S^m \tau) \right\rangle, \tag{2.6}$$

where stationarity has been assumed (i.e. the statistics of the fluctuating velocity field are independent of the time origin) and the asterisk denotes the complex conjugate. Next, we assume that the tensors, $\hat{S}_{ik}^n$ and $\hat{S}_{ik}^m$, are independent for $n \neq m$ and that the Fourier coefficients and ω_S^m are independent random variables:

$$\langle S_{ik}(0)\,S_{jl}(\tau)\rangle = \sum_{n=1}^{N} \langle \hat{S}_{ik}\,\hat{S}_{jl}^*\rangle \int_{-\infty}^{\infty} \exp(\mathrm{i}\pi\omega_S^n\tau)\,P(\omega_S^n)\,\mathrm{d}\omega_S^n, \tag{2.7}$$

where $P(\omega^n)$ is the p.d.f. of ω^n. The Fourier transform of (2.7) is:

$$\mathscr{F}(\langle S_{ik}(0)\,S_{jl}(\tau)\rangle) = \sum_{n=1}^{N} \langle \hat{S}_{ik}\,\hat{S}_{jl}^*\rangle \int_{-\infty}^{\infty}\int_{-\infty}^{\infty} \exp(\mathrm{i}\pi\omega_S^n\tau)\exp(-\mathrm{i}\pi\omega_S\tau)\,P(\omega_S^n)\,\mathrm{d}\omega_S^n\,\mathrm{d}\tau. \tag{2.8}$$

Orthogonality of the complex exponentials greatly simplifies (2.8) to:

$$\mathscr{F}(\langle S_{ik}(0)\,S_{jl}(\tau)\rangle) = N\langle \hat{S}_{ik}\,\hat{S}_{jl}^*\rangle\,P(\omega_S). \tag{2.9}$$

The autocorrelation function for the strain rate in isotropic turbulence derived in the Appendix is:

$$\langle S_{ik}(0)\,S_{jl}(t)\rangle = S_{ikjl}\exp\left(\frac{-t}{\tau_s}\right), \tag{2.10}$$

where $S_{ikjl} = \langle S_{ik}(0)\,S_{jl}(0)\rangle$ is the covariance of the strain rate given by (A 4). The exponential decay law given in (2.10) was found to represent the DNS data for the strain rate autocorrelation function accurately (Girimaji & Pope 1990). Coherent structures might be expected to give a long-time tail to (2.10), but Pope (1990) did not observe this for tensors – only for the magnitudes of the velocity gradient. Nonlinear regression of Girimaji & Pope's (1990) data based on (2.10) resulted in a strain rate correlation time, $\tau_S = 2.3/\Gamma_\eta$ with $r^2 = 99.5\%$. Similarly, the exponential decay fit the rotation rate autocorrelation function to yield a rotation rate correlation time, $\tau_R = 7.2/\Gamma_\eta$ with $r^2 = 95\%$. The Fourier transform of (2.10) gives:

$$\mathscr{F}(\langle S_{ik}(0)\,S_{jl}(\tau)\rangle) = \frac{2\tau_S\,S_{ikjl}}{1+(\pi\omega_S\tau_S)^2}. \tag{2.11}$$

Comparing (2.9) and (2.11), the p.d.f. of ω_S is chosen to be:

$$P(\omega_S) = \frac{\tau_S}{1+(\pi\omega_S\tau_S)^2}, \tag{2.12}$$

such that it satisfies the normalization condition, namely:

$$\int_{-\infty}^{\infty} P(\omega_S)\,\mathrm{d}\omega_S = 1. \tag{2.13}$$

The remaining terms in (2.9) and (2.11) specify the covariance of the random Fourier coefficients for the extensional flow component as:

$$\langle \hat{S}_{ik}\,\hat{S}_{jl}^*\rangle = \frac{2S_{ikjl}}{N}. \tag{2.14}$$

The strain rate autocorrelation function, (2.10), is a real, even function of time, leading to the constraint that the real and imaginary parts of $\hat{S}_{ik}$ are independent. For
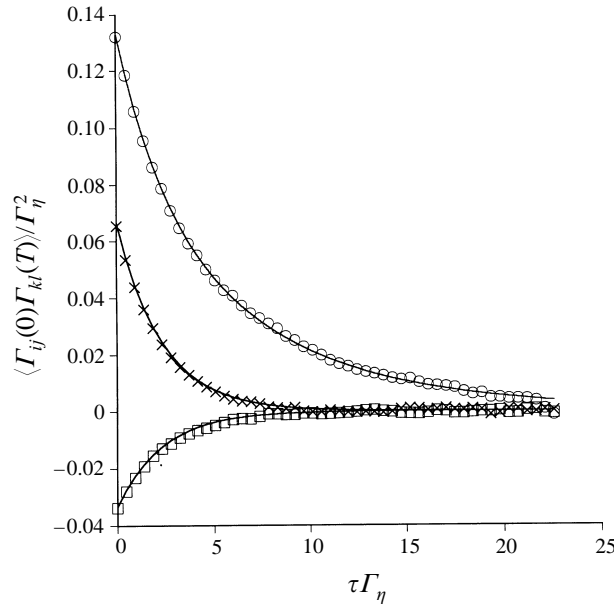
FIGURE 2. Three components of the fluctuating velocity gradient autocorrelation function as obtained by averaging 2000 realizations of the velocity gradient Fourier series representation. The random velocity gradient was represented by 200 Fourier modes. Components shown are $\bigcirc$, $\langle \Gamma_{11}\Gamma_{11}\rangle/\Gamma_\eta^2$; $\times$, $\langle \Gamma_{11}\Gamma_{22}\rangle/\Gamma_\eta^2$; $\square$, $\langle \Gamma_{12}\Gamma_{12}\rangle/\Gamma_\eta^2$. The simulation results show close agreement to the calculations based on DNS (solid lines).

simplicity, the variances of the real and imaginary parts are assumed to be equal. The restrictions imply that if:

$$\hat{S}_{ik} = A_{ik} + iB_{ik}, \tag{2.15}$$

then,

$$\left.\begin{aligned}
\langle A_{ik}B_{jl}\rangle = \langle B_{ik}A_{jl}\rangle = 0, \\
\langle A_{ik}A_{jl}\rangle = \langle B_{ik}B_{jl}\rangle = \frac{S_{ikjl}}{N}.
\end{aligned}\right\} \tag{2.16}$$

Similarly, the p.d.f. of ω_R and the variance of $\langle R_{ik}R_{jl}\rangle$ can be found. Final results for the rotational component of the Fourier series may be obtained by replacing S in equations (2.5)–(2.16) by R.

For each realization of the random flow, the Fourier coefficients defined by (2.4) were randomly picked from a joint normal distribution with zero mean and a variance satisfying (2.14)–(2.16). Similarly, the random frequencies for the specified strain and rotation rate correlation times were determined from the p.d.f.s defined in (2.12). Uniform and normally distributed random numbers used in describing a realization of $\Gamma_{ik}(t)$ were chosen using algorithms supplied in the *ranlib library* from NETLIB (Brown & Lovato 1996).

The Fourier series included enough terms so that, in the limit of many realizations, the specified second-order statistics of $\Gamma_{ij}(t)$ were obtained. Figure 2 shows three components of the velocity gradient autocorrelation coefficient calculated by averaging 2000 realizations of $\Gamma_{ij}(t)$ when N in (2.4) was 200. The solid lines are calculations derived from DNS for homogeneous isotropic turbulence (see Appendix; Girimaji & Pope 1990) and the symbols represent results obtained using the Fourier series

representation. The simulated fluctuating velocity gradient had autocorrelation functions that agreed quantitatively with the velocity gradient autocorrelation coefficients obtained from DNS.

2.2. *Constitutive relation for the interparticle potential*

A number of physicochemical forces can influence colloidal dynamics including van der Waals attraction, electrostatic double-layer repulsion and solvation forces (Stumm & Morgan 1981; Israelachvili 1992). We confine our analysis to destabilized colloidal systems where van der Waals attraction is the predominant colloidal force; however, the technique can be readily extended to include any colloidal force. In many systems, such as oceans and estuaries, particles are destabilized (Stumm & Morgan 1981) which means that electrostatic forces are negligible; therefore, including only van der Waals attraction in this analysis is not overly restrictive.

A van de Waals attractive potential corrected for retardation was used for the interparticle potential included in the equation of motion (2.1). Van der Waals attractions result from induced-dipole/induced-dipole interactions between neighbouring atoms. The pairwise sum of these attractions over a macroscopic body leads to a significant attractive potential that decays rapidly over distances comparable to the particle radius (Russel *et al.* 1989). Owing to the finite propagation speed of electromagnetic waves, dipole/dipole correlations between interacting atoms become out of phase at distances greater than the London retardation wavelength, λ, which further reduces the dispersion forces. In this work λ is set equal to 100 nm (van de Ven & Mason 1977; Davis 1984) in qualitative agreement with measurements (Suresh & Walz 1996). Schenkel & Kitchner (1960) provide an analytical approximation for the retarded van der Waals potential given by:

$$\phi_{vdw} = -\frac{A_H}{12(\xi + 0.885 N_L \xi^2)} \quad \text{for } \xi < 4/N_L, \tag{2.17}$$

$$\phi_{vdw} = -\left(\frac{A_H}{4\xi}\right)\left[\frac{4.9}{15 N_L \xi} - \frac{8.68}{45 N_L^2 \xi^2} + \frac{4.72}{105 N_L^3 \xi^3}\right] \quad \text{for } \xi > 4/N_L, \quad \xi \quad 1. \tag{2.18}$$

In (2.17) and (2.18), $\xi = (r - 2a)/a$ is the gap width scaled by the particle radius, A_H is the Hamaker constant, and N_L is the diameter of the two particles scaled by the London retardation wavelength: $N_L = 2\pi\sigma/\lambda$. These approximate expressions for the retarded van der Waals potential are valid in the limit of small separations (i.e. the lubrication regime). Constraining $\lambda \quad \frac{1}{2}\sigma$, so that van der Waals attraction decays in the lubrication regime, leads to the restriction that $N_L \quad 4\pi$, which is satisfied for all the particle sizes examined in this paper.

2.3. *Scaling*

Scaling of (2.1) is accomplished by normalizing the particle separation, r_i, with the particle radius, the time with the Kolmogorov time, and the velocity gradient with the Kolmogorov velocity gradient. Since the van der Waals attraction becomes significant for gap widths comparable to the London wavelength, the gradient of the potential scales with $A_H/4\lambda$. The final form of the equation of motion is:

$$\frac{\mathrm{d}r_i}{\mathrm{d}t} = \Gamma_{ik}(t)\, r_k - C_{ij}\, S_{jk}\, r_k - \frac{N_L}{8\pi N_S}\, M_{ij}\, \frac{\partial \phi(r)}{\partial r_j}, \tag{2.19}$$

Parameter	Interpretation	Magnitude
$\tau_S \Gamma_\eta,\ \tau_S \Gamma_\eta$	Total strain (rotation)	0 to ∞
$N_L = 4\pi a/\lambda$	Particle radius to London retardation wavelength	10^2 to 10^4
$N_S = 12\pi\mu a^3 \Gamma_\eta/A_H$	Viscous to van der Waals forces	$\sigma = 1\ \mu\mathrm{m}$: 10^{-3} to 10^3
		$\sigma = 100\ \mu\mathrm{m}$: 10^3 to 10^9

TABLE 1. Non-dimensional parameters and their typical magnitudes.

where N_s is defined in table 1 as the ratio of viscous to van der Waals forces. Hereinafter, scaled variables are used. Table 1 lists the expected magnitudes of the scaled parameters assuming an aqueous dispersion of 1–100 μm diameter colloidal particles with $\Gamma_\eta = 0.1$–$1000\ \mathrm{s}^{-1}$ and $A_H = 10^{-19}$–$10^{-21}\ \mathrm{J}$.

3. Turbulent coagulation for non-interacting particles

3.1. *Simulation procedure*

Simulations at arbitrary total strain and rotation were conducted in the absence of particle interactions to compare with the asymptotic limits provided by Saffman & Turner (1956) and Brunk *et al.* (1997*a*). The general simulation approach began by generating a realization of the random linear flow using the Fourier series method described in §2. The most obvious way to proceed would be to create particles at the outer simulation boundary such that the constant bulk concentration was maintained. Numerical integration could then be used to track the positions of the particles so that their rate of collision with the test sphere (as illustrated in figure 1) could be measured. However, since most particles in the bulk fluid (at $r = \infty$) do not collide with the test sphere in this approach, the efficiency of the numerical calculations would be low.

The efficiency of the computer simulations was greatly improved by running the simulation backwards in time. Instead of creating particles at $r = r_\infty$ and calculating the collision rate with the test particle, the particles were created at $r = \sigma$ and the simulation calculated the particle flow rate through the outer simulation boundary. Since the conservation equation for non-interacting particles is linear and time reversible, the flux calculated in the time reversed simulation was equal in magnitude to that obtained using the conventional boundary conditions shown in figure 1.

In the absence of particle interactions the equation of motion, (2.19), for the particles reduces to:

$$\frac{\mathrm{d}r_i}{\mathrm{d}t} = \Gamma_{ij}(t)\, r_j, \tag{3.1}$$

indicating that the particles follow the fluid motion. The only physical parameters that influence the coagulation dynamics in this case are the total strain and total rotation. In isotropic turbulence, the ratio of the strain rate to rotation rate is fixed because the turbulent dissipation rate is partitioned equally between the strain and rotational flow components; consequently, the effect of varying this ratio was not considered in the numerical analysis.

For each turbulent coagulation simulation, a unique realization of the spatially linear flow was generated using the Fourier series method outlined in §2.1. During each timestep the simulation checked to see if a particle should be created at the excluded volume surface. In the absence of interactions, particles follow the fluid motion;

therefore, the flux of pair probability at the particle surface is proportional to $C_1^2(\boldsymbol{u}\cdot\boldsymbol{n})$ when $|\boldsymbol{u}\cdot\boldsymbol{n}| > 0$ and the flux is zero otherwise. (Here, $\boldsymbol{n}$ is the outward pointing unit vector normal at the randomly chosen location, and $\boldsymbol{u}$ is the local velocity.) At locations of high local flux, the probability that a particle from the bulk enters the near field around the test particle is high, while the probability that a particle is swept into the simulation domain is low in regions of low volumetric flux. The probability of creating a particle is therefore proportional to the volumetric flux at the randomly chosen location:

$$P_{creation} = -\frac{\boldsymbol{u}\cdot\boldsymbol{n}}{(\boldsymbol{u}\cdot\boldsymbol{n})_{max}}, \qquad (3.2)$$

where $P_{creation}$ is the probability of creating a particle, and $(\boldsymbol{u}\cdot\boldsymbol{n})_{max}$ is the maximum volumetric flux that occurs at any position on the surface, $r = \sigma$, and at any time throughout the simulation. In the simulations, the maximum volumetric flux was estimated as $(\boldsymbol{u}\cdot\boldsymbol{n})_{max} \approx \sigma \langle \Gamma_{11}^2 \rangle^{1/2}$ and then refined by trial and error. The final estimate for $(\boldsymbol{u}\cdot\boldsymbol{n})_{max}$ was large enough for high shear fluctuations in the velocity gradient field not to lead to particle creation probabilities greater than 1. To evaluate (3.2), the simulation selected a random position on $r = \sigma$ using the acceptance–rejection technique developed by Von Neumann (1951) and computed the volumetric flux at the random location. If the calculated $P_{creation}$ was negative, a particle was not created since the volumetric flux was inward. For positive probabilities, the simulation created a particle if a uniform random number less than $P_{creation}$ was generated.

Although many particles existed within the control volume at any time, only encounters between a particle and the test sphere were considered. That is, the particles that were in relative motion around the test sphere passed through one another. In the physical application, the volume fraction of coagulating particles is very small so the likelihood of three-particle encounters is negligible. Simulating coagulation with higher-volume fractions but considering only two-particle interactions enhanced numerical efficiency while still reflecting the correct physics for a dilute suspension.

For each particle within the simulation domain, the equation of motion, (3.1), was integrated numerically using a fifth-order Runge–Kutta algorithm with adaptive timestep control. The maximum timestep allowed was set at the period of the fastest Fourier mode, so the Runge–Kutta scheme resolved this mode with a minimum of five intermediate timesteps. The permissible integration error was established by balancing the penalty for evaluating (2.4) at many timesteps with the requirement that non-interacting particles follow the streamlines of the flow. To set the maximum integration error, we used calculations performed in a steady strain field. Ideally, in the steady flow, all particles should reach $r = r_\infty$ since they are created in regions of outward-going flux. When the integration error was too large, some particles crossed the streamlines of the flow and returned to the test sphere. A maximum local integration error equal to 1% of the relative particle separation distance was found to eliminate streamline crossing.

Particles that reached $r = r_\infty$ or returned to $r = \sigma$ were removed from the simulation. The average particle flow rate through the system, Q, was calculated as the total number of particles that reached the outer simulation boundary divided by the total simulation time. Statistics on Q and the radial pair probability density profile were obtained at intervals of τ_∞, the characteristic time for a particle to travel from r_∞ to σ. In the large total strain limit, τ_∞ scales with the Kolmogorov time; however, in the diffusion limit it can take much longer for particles to reach the test sphere. When diffusion dominates the system, τ_∞ is estimated by relating the radial components of

the turbulent diffusivity given by (1.7) to half of the time derivative of the mean square displacement to obtain (Russel *et al.* 1989):

$$\frac{1}{2}\frac{\mathrm{d}\langle r^2 \rangle}{\mathrm{d}t} = \frac{\tau_S \Gamma_\eta}{15}\langle r^2 \rangle. \tag{3.3}$$

This ODE for the mean square displacement was integrated to estimate the characteristic time for particles to diffuse from $r = \sigma$ to $r = r_\infty$ as:

$$\tau_\infty = \left(\frac{1}{\tau_S \Gamma_\eta}\right)\ln\left(\frac{r_\infty^2}{\sigma^2}\right). \tag{3.4}$$

In the computer simulations, characteristic times were estimated for both the small and large total strain limit, and the longer of the two was used as τ_∞ for the simulation.

Each realization of the flow field was simulated until the particle flux at the excluded volume surface and the outer simulation boundary differed by less than 2% from their values at the previous τ_∞. A simulation typically achieved steady state in less than 20 characteristic times.

At steady state, the net flux of particles entering at the surface of the excluded volume ($r = \sigma$) is constant and can be written as:

$$C_1\langle \boldsymbol{u}\cdot\boldsymbol{n}\rangle = \frac{1}{\pi\sigma^2}\left(\frac{\langle \boldsymbol{u}\cdot\boldsymbol{n}\rangle}{(\boldsymbol{u}\cdot\boldsymbol{n})_{max}}\right). \tag{3.5}$$

The right-hand side of (3.5) can be interpreted as the product of the maximum particle flux at the excluded volume surface for the test particle (the maximum particle flux is one particle created over the surface of the excluded volume per timestep or $1/\pi\sigma^2$) and the average probability of creating a particle during a timestep. Solving for C_1 yields:

$$C_1 = \frac{1}{\pi\sigma^2(\boldsymbol{u}\cdot\boldsymbol{n})_{max}}. \tag{3.6}$$

The coagulation kernel for each realization was calculated as $k^0 = Q/C_1$.

For each set of system parameters the coagulation rate constant was obtained by ensemble averaging over independent realizations to achieve the desired level of accuracy. For the simulations with non-interacting particles, ensemble averaging continued until the standard deviation of k^0 was less than 2% of its mean value. The number of realizations required to achieve good statistics varied strongly with total strain. For total strains less than 1, as few as 10 realizations were needed, while at total strains greater than 10, nearly 1000 realizations were required to achieve low statistical errors. At small total strain, particles experience a rapidly fluctuating flow so that net particle movement is the result of many uncorrelated normally distributed velocity gradient fields. In effect, coagulation results are time and also ensemble averaged in this limit. In contrast, at the large strain limit, the flow field varies slowly and particles experience a nearly stationary flow; thus, obtaining good statistics depended solely on ensemble averaging over many realizations.

Along with the parameters summarized in table 1, the outer simulation boundary, r_∞, the maximum volumetric flux at r_∞ and the number of Fourier modes, N, were specified at the beginning of a simulation. Initial computations were conducted to investigate the effect of the simulation parameters on the reported results. For most coagulation simulations, we truncated the Fourier series used to represent the fluctuating velocity gradient field at 300 Fourier modes. The effect of N was evaluated
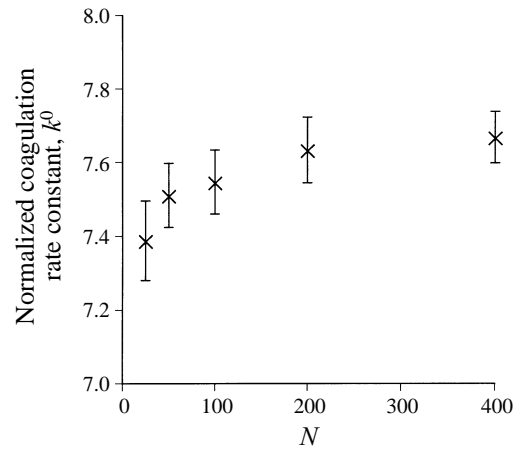
FIGURE 3. The effect of N on the ensemble average of the turbulent coagulation kernel for 100 realizations of the system. Error bars denote $\pm$ one standard deviation.

by simulating isotropic turbulence ($\tau_S \Gamma_\eta = 2.3$ and $\tau_R \Gamma_\eta = 7.2$) while varying the number of components in the Fourier series from $N = 25$ to $N = 400$. For this simulation series, the maximum particle flux was held constant and each data point represented the average of 100 realizations. To facilitate comparison, statistical fluctuations were reduced by starting each member of the simulation set with the same random number generator seeds. In this way, velocity gradient field Fourier modes present in all the simulations were the same and the random numbers sampled when introducing new particles were identical.

Figure 3 summarizes the results by plotting normalized coagulation rate against the number of elements in the Fourier series. The error bars denote $\pm$ one standard deviation. The normalized rate constant, k, monotonically increased towards an asymptotic value as N was increased. The normalized coagulation rate rose 3.7% when increasing N from 25 to 200, while k grew only 0.4% when N doubled from 200 to 400. Statistical error decreased with increasing N, from a coefficient of variation (i.e. the standard deviation divided by the mean) of 1.4% at $N = 25$ to 1.2% at $N = 200$, and to 0.9% at $N = 400$. The decrease in statistical uncertainty was presumed to occur because the p.d.f. of each flow realization was better approximated by a Gaussian distribution at large N. Given the magnitude of the coefficient of variation for k^0, the marginal improvement gained from increasing $N = 200$ to $N = 400$ was not deemed to be significant.

The outer simulation limit was chosen to minimize boundary effects. In the limit of large total strain, curved streamlines that exit and re-enter the simulation control volume may exist. Particles that exit the simulation boundary cannot re-enter, this would lead to a higher than expected net flux through the outer simulation boundary. Simulations conducted in the persistent strain limit for r_∞ ranging from 5 to 30 resulted in computed coagulation rates that were not statistically different. Therefore, recirculating streamlines broken by the finite simulation boundary were not consequential when estimating the collision rate for $r_\infty > 5$.

The effect of the finite simulation volume is anticipated to be largest in the limit of small total strain where the turbulent coagulation process is diffusive. To compute the boundary effect in the small total strain limit, we solve the radial component of the pair probability equation with absorbing boundary conditions at the inner and outer
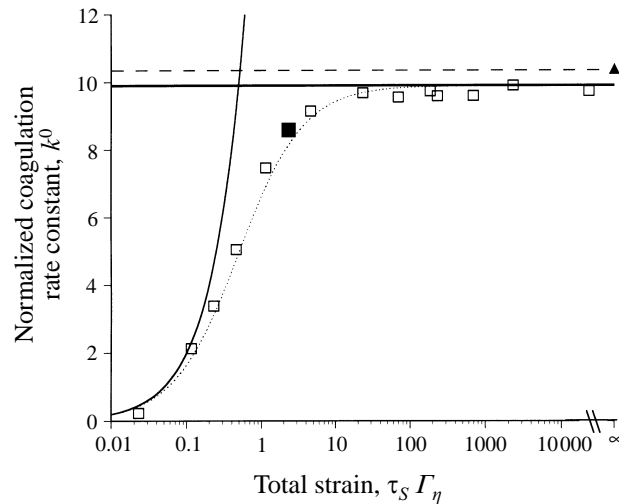
FIGURE 4. The effect of simultaneously varying $\tau_S \Gamma_\eta$ and $\tau_R \Gamma_\eta$ on the normalized turbulent coagulation rate constant. In these simulations the ratio of total rotation to total strain was fixed at the value 3.13 obtained from analysis of the DNS data. □, simulation data; ■, prediction for isotropic turbulence ($\tau_S \Gamma_\eta = 2.3$, $\tau_R \Gamma_\eta = 7.2$). Unless shown, the $\pm$ one standard deviation error bars on the simulation results are smaller than the symbols. Asymptotic limits for small total strain (thin line), large total strain (thick line), and the Saffman & Turner (1956) predication (dashed line) are also shown. Simulations performed at infinite total strain and rotation are shown with (thick solid line) and without (▲) the effects of rotation. An interpolation of the asymptotes (3.8) shown as the dotted line closely approximates the simulation data.

simulation boundary (see Brunk *et al.* 1997). The resulting steady state coagulation rate constant normalized by the particle radius and Kolmogorov shear rate is:

$$k^0 = \frac{32\pi}{5} \tau_S \, \Gamma_\eta \left[\frac{r_\infty^3}{r_\infty^3 - \sigma^3} \right]. \qquad (3.7)$$

The term in brackets is the contribution of the finite outer boundary to the calculated coagulation rate constant. For most simulations discussed below, $r_\infty = 10$. With $r_\infty = 10$, the coagulation kernel in the diffusive limit increases about 0.8% above that for an infinite domain. An error of 0.8% is negligible compared to the statistical error in the calculations and has been ignored in the ensuing analysis.

At intermediate strain the effect of the outer simulation boundary was surmised to lie between the large and small strain extremes; therefore, we use the magnitude of boundary effects at the small strain limit to set an appropriate outer simulation boundary so that the outer boundary had a negligible influence on the numerical calculations.

3.2. *Simulation results*

In this section the effect of varying the total strain and rotation on the coagulation rate is discussed and we contrast the simulation results with the analytical solutions for large and small total strain limits that are summarized in §1. Additional simulations investigate the effect of the total rotation on the rate of particle coagulation.

Figure 4 illustrates how the coagulation kernel normalized with the Kolmogorov shear rate and particle radius changes when $\tau_S \Gamma_\eta$ and $\tau_R \Gamma_\eta$ are varied while maintaining $\tau_S \Gamma_\eta / \tau_R \Gamma_\eta = 0.32$, corresponding to isotropic turbulence. The square symbols represent the simulation data, and unless otherwise shown, the standard

deviations of the data points are smaller than the symbols. The symbol denoted by the solid square represents the expected physical state of isotropic turbulence as estimated from DNS data ($\tau_S \Gamma_\eta = 2.3$ and $\tau_R \Gamma_\eta = 7.2$). Also shown are the asymptotic limits of large (thick solid line) and small (thin solid line) total strain. At small total strain the pair diffusion formulation (Brunk *et al.* 1997), given by (1.8), is valid and $k^0 = 32\pi\tau_S \Gamma_\eta/5$ in normalized form. The simulations reach 95% of the pair diffusion limit by $\tau_S \Gamma_\eta = 0.115$ (see figure 4). With increasing total strain, the simulation results increase until, at a total strain of about 10, the calculated k^0 levels off and becomes independent of the applied total strain. The large total strain asymptotic limit was estimated by running simulations with an infinite total strain and rotation (i.e. the flow is stationary). At large total strain we find (thick horizontal line on figure 4) that $k^0 = 9.896 \pm 0.0805$. By $\tau_S \Gamma_\eta = 23$ and $\tau_R \Gamma_\eta = 72$ the simulations are within 98% of the asymptote.

The Saffman & Turner model prediction in the large strain limit, (1.6), is $k^0 = 10.36$ in non-dimensional form and is shown as the dashed line on figure 4. It is evident that this model overestimates the actual coagulation rate in the large strain limit by about 5%. A *z*-test shows that the difference between the infinite total strain simulation results and Saffman & Turner model's predictions is statistically significant (*p* value $= 10^{-8}$). In Saffman & Turner's theoretical analysis the local turbulent velocity field is represented as a linear irrotational flow, while the simulations described here include both strain and rotational components of the velocity field. Considering the effects of strain and rotation separately, one expects the rate of coagulation to be independent of rotation because a solid body rotation, by itself, does not cause a net flux of particles towards the test sphere. The simulation results, however, indicate that the effects of rotation and extension are not superimposable in coagulation. To confirm this possibility, computer simulations were run at infinite total strain in a purely extensional flow. The ensemble averaged coagulation rate, shown by the triangle on figure 4, falls on the Saffman & Turner prediction and a *z*-test reveals that the simulation prediction for k^0 is not statistically different from the Saffman & Turner prediction of 10.36 (*p* value = 0.46). When simulating an irrotational flow, the computed turbulent coagulation agrees with the Saffman & Turner large total strain asymptote; therefore, the addition of rotation must decrease the turbulent shear coagulation rate.

The reason that strain and rotation are not superimposable is that the combination can lead to particle trajectories that leave and later return to the excluded volume surface and thus contribute no particle flux. Although one can superimpose strain and rotation when calculating the flow into $r = \sigma$, adding rotation to the pure straining flow field leads to recirculating trajectories having no net contribution to the coagulation rate. It follows that the coagulation rate is overstated in an analysis that neglects rotation. This effect is explored in more detail below.

For isotropic turbulence ($\tau_S \Gamma_\eta = 2.3$ and $\tau_R \Gamma_\eta = 7.2$), we calculate a value of $k^0 = 8.62 \pm 0.02$ for the normalized coagulation kernel. The Saffman & Turner model prediction of 10.36 overestimates the true coagulation rate by 20%. Similarly, the diffusion approximation, (1.8), evaluated at $\tau_S \Gamma_\eta = 2.3$, estimates the normalized coagulation rate to be 46.24, approximately 5 times larger than the actual value. Although the asymptotic limits fail to predict the turbulent coagulation rate for isotropic turbulence, they can be used to construct an interpolation of the simulation data. A hyperbolic approximation of the following form is used to interpolate between the asymptotic solutions:

$$k^0 = \frac{P_1 \tau_S \Gamma_\eta}{1 + Q_1 \tau_S \Gamma_\eta}. \tag{3.8}$$

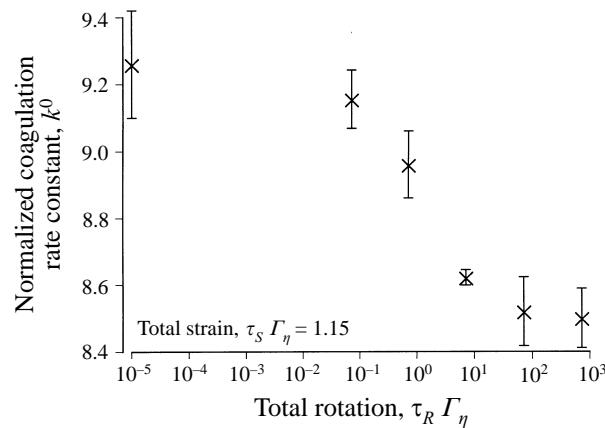FIGURE 5. The normalized coagulation rate constant as a function of the rotation rate correlation time while keeping $\tau_S \Gamma_\eta = 1.15$. Error bars are $\pm$ one standard deviation from the mean.

Applying the small and large total strain asymptotic limits to (3.8) leads to $P_1 = 32\pi/5$ and $Q_1 = 0.65\pi$. This interpolation, shown as the dotted line in figure 4, closely approximates the simulation data to within an error of 5%.

Perhaps one of the most interesting aspects of these results is that the addition of rotation can cause a decrease in the coagulation rate. The effect of rotation has been previously identified in stationary linear flows (Greene, Hammer & Olbricht 1994; Zeichner & Schowalter 1977). Zeichner & Schowalter (1977) derive the coagulation rate in a uniaxial extensional flow (a pure strain field) and compare the results with coagulation in simple shear (a flow that contains rotation) with and without interparticle interactions. For the same rate of strain, they find that the k^0 for simple shear is about 3.5 times smaller than the k^0 calculated for uniaxial extension. In the same vein, Greene *et al.* (1994) note that linear flows with high vorticity have closed streamlines and that these closed streamlines can be expected to substantially decrease the kinematics of particle aggregation. Since the turbulent flow field in the neighbourhood of a test particle can be conceptualized as an ensemble average overall possible linear flows, we expect the coagulation rate to be lower than is predicted in the absence of rotation.

The correlation time for the rotation rate can also be anticipated to influence the coagulation rate. When the rotation is persistent (i.e. the total rotation is large) recirculating streamlines present in the flow can be expected to endure and thus the coagulation rate would be lower. Conversely, when the rotation rate correlation time is small, the location of streamlines that return to the excluded volume fluctuates and the effect of the curved streamlines is expected to be mitigated. Numerical simulations run at $\tau_S \Gamma_\eta = 1.15$ and various $\tau_R \Gamma_\eta$ illustrate the effects of persistent rotation. The normalized coagulation rate constants for values of τ_R ranging from 0 to 720 are shown in figure 5. Each simulation set started with the same random seeds to facilitate comparison and enough realizations were computed to achieve a coefficient of variation less than 2%. The normalized coagulation rate constant, k^0, ranged from 9.26 ± 0.16 at $\tau_R = 0$ to 8.50 ± 0.09 at $\tau_R = 720$. Increasing the rotation rate correlation time decreased the calculated k^0 to about 92% of its maximum value, in agreement with expectations.

Pair probability distributions for three simulation conditions and analytical results for the small total strain limit (diffusion limit) are compared in figure 6. Computed pair
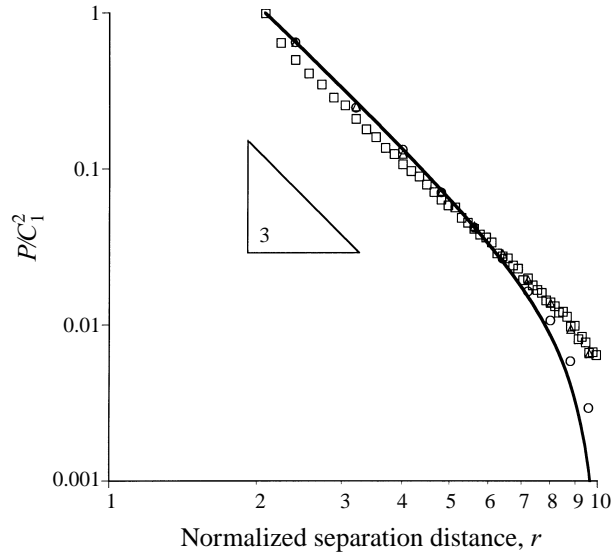
FIGURE 6. Radial concentration profiles calculated for $\bigcirc$, $(\tau_S \Gamma_\eta, \tau_R \Gamma_\eta) = (0.23, 0.72)$; $\triangle$, $(2.3, 7.2)$; $\square$, (∞, ∞). The solid line represents the analytical prediction valid in the limit of small total strain.

probability profiles are shown for $(\tau_S \Gamma_\eta, \tau_R \Gamma_\eta) = (0.23, 0.72)$ (circles), $(2.3, 7.2)$ (triangles) and (∞, ∞) (squares). For pure convection (large total strain), where the relative velocity is proportional to the separation distance, $P(r)$ is expected to decay in proportion to $1/r^3$. Similarly in the small total strain limit we expect a $1/r^3$ decay since the turbulent diffusion coefficient is proportional to the separation distance squared. Hence, it is not surprising that each simulation condition shown in figure 6 has the $1/r^3$ dependence in the pair probability. The concentration distributions obtained at larger correlation times have discontinuous drops to zero concentration at the boundaries of the simulation domain. As the correlation times decrease and the relative particle motion becomes more diffusive, the concentration profile at the domain boundaries begins to decrease faster than $1/r^3$. The profile in the diffusion limit can be found as a solution to a pair probability equation using the diffusivity given by (1.7) to represent transport due to turbulence. The pair probability in the small total strain limit has the following form in the presence of the outer boundary:

$$\frac{P}{C_1^2} = \frac{8}{r^3}\left(\frac{r_\infty^3 - r^3}{r_\infty^3 - 8}\right), \tag{3.9}$$

where the term in parentheses corrects for the finite size of the computational domain. Results for $\tau_S \Gamma_\eta \to 0$, $\tau_R \Gamma_\eta \to 0$ are shown as the solid line in figure 6. Effects of the finite outer boundary became important at about $r = 7$ in the small total strain limit and are characterized by a more rapid decrease in the concentration relative to the $1/r^3$ decay. This behaviour is closely matched by the $(\tau_S \Gamma_\eta, \tau_R \Gamma_\eta) = (0.23, 0.72)$ simulations shown with the circles.

4. Turbulent coagulation for interacting particles

It is reasonable to expect that particle interactions such as hydrodynamic interactions and van der Waals forces will affect the turbulent coagulation rate. Hydrodynamic interactions are the result of viscous drag on the colloidal particles and the lubrication

forces that amass in the gap between two colliding particles. Without a compensating attractive interparticle force, hydrodynamic interactions prevent particle collision. At small particle separations, attraction due to dispersion (i.e. van der Waals) forces can overcome the viscous resistance to collision and lead to particle contact. The inclusion of these two forces into the coagulation kernel provides the minimum requirements to predict experimental results. In this section, we first describe alterations to the simulation procedure – most notably, the simulations must be performed by a less efficient forward integration in time. Then the effects of varying the particle size, relative strength of van der Waals to hydrodynamic forces and the total strain (rotation) are examined.

4.1. *Simulation method*

In contrast to the situation without particle interactions, the particle conservation equation is neither linear nor time reversible when interactions are included. This means the efficient time-reversed simulation method used in the non-interacting case (see §3.1) can no longer be employed. Instead, the coagulation rate constant was calculated from the trajectories of particles released at $r = r_\infty$ that reached the excluded volume surface of the test sphere. For large values of r_∞, this methodology became very inefficient as most particles created at the outer simulation boundary left the simulation domain without interacting with the test particle. The efficiency of the calculation was improved by decreasing r_∞; however, this came at the expense of computational accuracy, as described in §3.1.

In these simulations $r_\infty = 5$ was selected as a compromise between the error resulting from using a small simulation domain and the inefficiency of the forward time numerical computations for large simulation domains. As discussed in §3.1, the finite value of r_∞ can affect the calculated value of k^0 in the diffusion limit. Using (3.7), k^0 is expected to be overestimated by as much as 6 % as the total strain is decreased. Simulations of non-interacting particles conducted at several values of $\tau_S \Gamma_\eta$ and $\tau_R \Gamma_\eta$ were used to develop correlations for the finite box size. Using simulations for non-interacting particles to assess the effect of r_∞ was deemed to be reasonable because interactions were weak at $5 < r_\infty < 10$. For each total strain examined, several realizations at $r_\infty = 5$ and $r_\infty = 10$ were computed using the same random number seeds to minimize statistical fluctuations. Using $r_\infty = 5$ had less than a 2 % effect, with the impact decreasing with increasing total strain. This result suggests that the smallest total strain examined in the simulations was larger than that required for the pair diffusion formulation to become valid. Corrections of the order of 2 % were not considered to be statistically significant, so the simulation results obtained with $r_\infty = 5$ are presented here without correction.

For the case of interacting particles, the computer program generated a unique realization of the flow field and computed the relative trajectories of the particles using the full equation of particle motion given by (2.19). At each timestep, a modified form of (3.2) was used to determine if a particle should be created at $r = r_\infty$. Instead of evaluating (3.2) using the hydrodynamic conditions at $r = \sigma$, the local flux was evaluated at $r = r_\infty$ and $(\boldsymbol{u} \cdot \boldsymbol{n})_{max} \approx r_\infty \langle \Gamma_{11}^2 \rangle^{1/2}$. This methodology for particle creation assumed that at large separations the particles follow the fluid motion, so the flux at the outer simulation boundary was accurately represented by $(\boldsymbol{u} \cdot \boldsymbol{n}) C_1$. Indeed, at $r = 5$ the hydrodynamic interactions due to a linear flow have only a 3.5 % effect on the particle radial velocity while van der Waals forces between a newly created particle and the test sphere are negligible.

The simulation tracked the particles until they either collided with the test sphere or

left the simulation boundary. Statistics on the average influx of particles through the excluded volume surface, Q, were collected periodically until steady state was reached. The program then computed the average coagulation rate for each flow field realization as before using the relation $k = Q/C_1$ where the particle concentration at $r = r_\infty$, was given by (3.6) evaluated at r_∞ rather than σ.

We anticipated that traversing the lubrication regime, where the gap thickness is small compared to the particle radius and hydrodynamic forces are significant, would be the rate limiting step for coagulation. Therefore, it was essential that the simulations accurately resolved the motion at small particle separations. The maximum local integration error of 1% set previously also kept the simulation sufficiently accurate in the lubrication region. When two particles were separated by small gap widths, the timestep was automatically refined by the error control algorithm to reflect the large van-der-Waals- and hydrodynamic-induced particle fluxes.

Adding interparticle interactions led to another difficulty, namely at particle contact both the hydrodynamic interaction and the van der Waals forces diverge. The singularities in the van der Waals and hydrodynamic interactions were avoided by choosing a collision radius slightly larger than the particle diameter, $r = \sigma + 0.01\lambda$. At this particle separation, the relative particle velocity induced by the van der Waals attraction overwhelmed effects of the flow resistance and the particles always collided in the next timestep.

4.2. *Simulation results*

Along with the total strain and rotation, two additional parameters govern the coagulation dynamics in systems with particle interactions, namely: the shear number, N_S, describing the relative importance of viscous and van der Waals forces, and N_L, the ratio of the particle radius to the London retardation wavelength (i.e. the lengthscale over which van der Waals attraction decays) (see table 1). In this section we consider the effects of varying the shear number and particle size for coagulation in isotropic turbulence. The effect of varying the total strain and rotation on the coagulation rate constant and the collision efficiency for a single particle size and shear number are also evaluated.

Simulations in isotropic turbulence ($\tau_S \Gamma_\eta = 2.3$ and $\tau_R \Gamma_\eta = 7.2$) were run for $N_L = 237$, 474 and 4740 corresponding to 3.9, 7.6 and 76 µm diameter particles in a flow characterized by N_S ranging from 10^{-1} to 10^9. Results from these simulations, plotted as the collision efficiency, α, versus N_S, are shown in figure 7 along with error bars denoting $\pm$ one standard deviation. The results indicate that the effect of particle interactions is significant. For the parameter range investigated, the collision efficiency is smaller than about 50%, indicating that fewer than 1 out of 2 collisions that occur in the non-interacting case actually transpire when particle interactions are included in the analysis. Increasing the particle size adversely affects the collision efficiency because lubrication forces are more significant for larger particles. For each particle size the collision efficiency goes through a maximum at a critical $N_S = N_S^*$ that depends on the particle size. Within the error, the data for all three particle sizes collapses onto a single curve to the right of the maximums.

The maximum in the collision efficiency indicates that there is an optimal combination of shear rate and particle size that results in the most efficient coagulation. The interplay of mechanisms that leads to the maximum in the collision efficiency for each particle size can be understood by considering the relative velocity due to turbulent shear and the van der Waals force at separations where the van der Waals force becomes significant. At this gap width, van der Waals attractions have sufficient
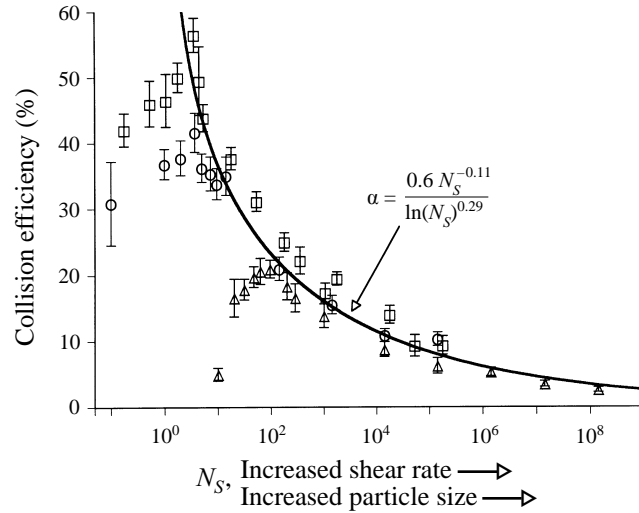
FIGURE 7. The collision efficiency, α, as a function of the shear number, N_s, for various particle sizes (N_L). $\square$, $a = 1.9\ \mu\text{m}$; $\bigcirc$, $3.8\ \mu\text{m}$; $\triangle$, $38\ \mu\text{m}$. The error bars are $\pm$ one standard deviation. The power law fit was obtained by non-linear regression of the data to the right of the maximums.

magnitude to draw the particles together. Depending on the particle size, the critical gap width scales with either the London retardation length or, if the particles are small enough, the lengthscale at which lubrication forces break down. In the lubrication regime (i.e. $\xi \quad 1$), the velocity due to the fluid shear, V_S is proportional to $\Gamma_\eta \sigma(1 - A(r))$ where the lubrication resistance to motion, $1 - A(r)$, is 4.077ξ (Russel *et al.* 1989). Furthermore, the relative particle velocity due to the van der Waals force scales in proportion to $V_{VDW} \sim A_H G(r)/12\pi\mu\xi^2$, where the lubrication resistance to motion $G(r) = 2\xi$ (Russel *et al.* 1989). Balancing these two velocities yields:

$$\frac{V_S}{V_{VDW}} \sim C^2 \xi^{*2} N_{S*}, \tag{4.1}$$

where ξ^* is the critical gap width at which van der Waals forces become important and it is defined as the minimum of $4\pi/N_L$ and 0.1. $\xi^* = 4\pi/N_L$ corresponds to a gap width of λ and $\xi^* = 0.1$ is meant to characterize the gap width at which lubrication forces break down, $0.1a$. N_S^* in (4.1) is the critical shear number that gives the maximum collision efficiency, and C is a constant found to be about 10 when balancing the turbulent shear and van der Waals attraction. When $C^2 \xi^{*2} N_S = 1$, the turbulent shear is just strong enough to bring the particles to the gap widths where van der Waals forces dominate and collision is assured. For $C^2 \xi^{*2} N_S > 1$, particle motion due to turbulence dominates van der Waals forces, so particles are pushed toward smaller gap widths before van der Waals forces take over and allow the particles to collide. Since lubrication resistance is more significant at small gap widths, the collision efficiency decreases. When $N_S > N_S^*$, figure 7 shows that the collision efficiency is nearly independent of the particle size (i.e. independent of N_L). This is because the point at which van der Waals forces take over from the lubrication force and draws the particles together is much smaller than the retardation length, so λ and hence N_L become irrelevant. At the opposite extreme, when $C^2 \xi^{*2} N_S < 1$, turbulent shear is too weak to transport the particle to gap widths comparable to ξ^*. As a result, van der Waals forces are unable to cause particle collision and the collision efficiency declines.
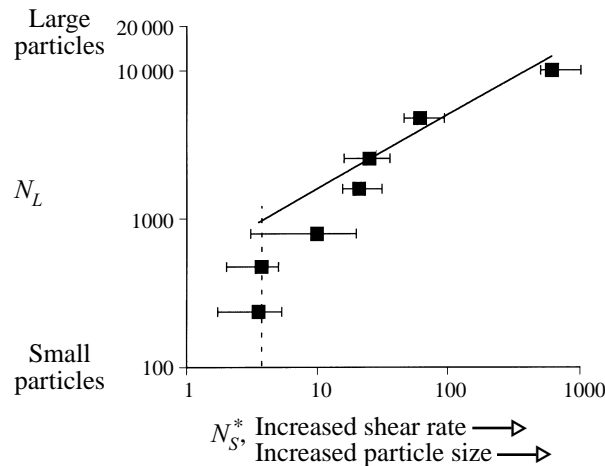
FIGURE 8. The dependence of the particle size (N_L) on the critical shear number, N_S^*, at which the collision efficiency goes through a maximum. The lines are scaling predictions assuming that flux due to the velocity gradient field and that due to the van der Waals attraction are balanced at the maximum collision efficiency. The solid line applies to large particles where the characteristic lengthscale for the van der Waals attractions scales with the London retardation length. The dashed line applies for small particles where the particle radius provides the correct lengthscale for the van der Waals attraction.

The region of applicability of the force balance given by (4.1) is illustrated in figure 8. Here the critical $N_S = N_S^*$ is plotted against N_L, where N_L is the ratio of the particle size to the London wavelength (see table 1). The critical shear number dependence on N_L is shown for the three particle sizes given in figure 7 as well as for particle diameters of 12.5, 25, 40 and 159 µm. The solid line with $C = 40$ is the prediction for N_S^* valid when λ characterizes the distance at which van der Waals forces becomes important. As N_L decreases, the particle radius rather than the London retardation length is the appropriate scaling for the van der Waals force. Letting $\xi^* = 0.1$ and $C = 20$ gives the dashed line. The critical shear number prediction given by the solid line works well for the large particles (i.e. $N_L \gtrsim 2000$), but it underestimates N_S^* for $N_L \lesssim 2000$. For the two smallest particles ($\sigma = 3.9$ and 7.8 µm) simulated, N_S^* seems to be independent of N_L, in agreement with the scaling that uses the particle radius as the characteristic lengthscale for the van der Waals forces.

The scaling relation developed above to explain the maximum in the collision efficiency curves is based upon the concept that the van der Waals attraction force acts to draw particles together once the turbulence has transported them to a critical separation distance. For shear numbers above the critical value, the turbulence has sufficient strength to bring the particle pair to separations smaller than λ, beyond which point, van der Waals attractions inevitably cause a particle collision. It follows that the collision efficiency could be estimated by calculating the particle flux through the critical separation distance ($\xi = \xi^*$) by using an estimate for the pair probability based upon hydrodynamically interacting particles. This analysis assumes that the pair probability is unperturbed by the van der Waals attraction for gap widths larger than the critical separation, so the effect of van der Waals attractions can be ignored when estimating the pair probability. For $N_S > N_S^*$, the gap width at which the shear and van der Waals forces balance is less than the London wavelength; therefore, we can restrict consideration to the non-retarded van der Waals potential and the lubrication region. Batchelor & Green (1972*a*, *b*) derived the pair probability for particles influenced by

hydrodynamic interactions in a linear flow. In the lubrication regime (ξ 1) they obtained:

$$P(\xi) \approx \frac{0.234 C_1^2}{\xi^{0.781}[\ln(1/\xi)]^{0.29}}, \qquad (4.2)$$

as before, C_1^2 is the pair probability of singlet particles at large particle separations. Although this result is applicable to linear flow fields with open streamlines, we will use it to interpret our simulation result for the unsteady turbulent flow.

An estimate for α may be obtained by taking the ratio of the particle flux at ξ^* with hydrodynamic interactions to the particle flux in the absence of particle interactions. The critical gap width, ξ^*, is given by the flux balance used to calculate (4.1). We find that $\xi^* \sim N_S^{1/2}$ and, after some manipulation, the following prediction for the collision efficiency results:

$$\alpha = \alpha^0 \frac{N_S^{-0.11}}{[\ln(N_S)]^{0.29}}, \qquad (4.3)$$

where α^0 is an order one constant. The solid line in figure 7 is the collision efficiency predicted using (4.3), where $\alpha^0 = 0.6$. For the simulation data to the right of the maximum, $N_S > N_L^2/C^2$, (4.3) fits the data with $r^2 = 94\%$. By assuming the primary contribution to the collision efficiency comes from the difference in the pair probability with and without hydrodynamic interactions, (4.3) is able to predict the variation of α with the shear number.

For subsequent comparison with other calculations, it is useful to note that for $N_S > 10$ and $N_S > N_S^*$, (4.3) behaves like a power law of the form:

$$\alpha = 0.52 N_S^{-0.16}. \qquad (4.4)$$

Since the normalized coagulation kernel is $k = \alpha k^0$, this implies that the coagulation rate constant increases with $\Gamma_\eta^{0.84}$ for isotropic turbulence. Comparing this estimate with values predicted for the asymptotic limits of small and large total strain is worthwhile. Predictions derived for non-Brownian particles in the small strain limit indicate that $k \sim \Gamma_\eta^{0.89}$ (Brunk *et al.* 1997*a*). Compared with the moderate total strain result, coagulation is slightly less retarded by particle interactions in the diffusion limit. As previously noted, the presence of hydrodynamic drift that brings the particles close together increases the collision efficiencies in the small strain limit (Brunk *et al.* 1997*a*). To our knowledge, the effects of particle–particle interactions have not been computed for turbulent flows in the limit of large total strain. Computations of collision efficiencies in steady linear flows, however, are prevalent (Greene *et al.* 1994; van de Ven & Mason 1977; Zeichner & Schowalter 1977; Adler 1981). Recent trajectory calculations computed for a number of steady linear flows have shown that the stability factor for flows with more strain than vorticity is nearly insensitive to flow type, except for flows similar to simple shear (Greene *et al.* 1994). In the large total strain limit, the pseudostationary linear flow field around a test particle can be conceptualized as an ensemble average over all possible linear flows; therefore, the collision efficiency in the large strain limit is expected to correspond to the average collision efficiency for all possible steady linear flows. Based upon Greene *et al.*'s conclusion that collision efficiency is insensitive to flow type, values of α calculated for simple shear and uniaxial extension are considered. Zeichner & Schowalter (1977) calculated the stability factors for uniaxial extension and simple shear for particles influenced by retarded van der Waals attraction and hydrodynamic interactions. An examination of their computations reveals that k is proportional to $\Gamma_\eta^{0.77}$ for simple shear (using the correction
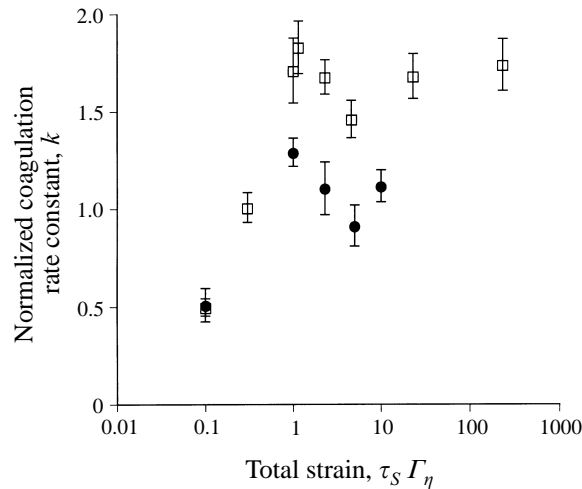
FIGURE 9. The coagulation rate constant against the total strain for 1.9 μm radius particles and □, $N_S = 1761$; ●, $N_S = 17610$. Symbols represent the simulation data and the error bars are $\pm$ one standard deviation from the mean. Results are for a fixed ratio of total rotation to total strain equal to 3.13.

published in Feke & Schowalter 1983) and $\Gamma_\eta^{0.89}$ for uniaxial extension. In isotropic turbulence ($\tau_S \Gamma_\eta = 2.3$ and $\tau_R \Gamma_\eta = 7.2$), the dependence of k on the shear rate is intermediate between the steady linear flow cases.

Based on the above analysis, variations of the coagulation rate constant can be predicted as a function of the total strain when the shear number and particle size are held constant. In the small total strain limit the asymptotic approximation valid when the interparticle forces decay in the lubrication regime gives the normalized coagulation rate constant, $k \approx 0.25(\tau_S \Gamma_\eta)^{0.11} N_S^{0.11}$ (Brunk *et al.* 1997). The estimate for isotropic turbulence comes from combining $k^0 = 8.62$ and (4.2) to yield $k \approx 5N_S^{0.84}$. At large total strain, $k^0 = 9.96$ and we obtain $k \approx 5.6N_S^{0.77 \text{ to } 0.89}$, where the collision efficiency pre-exponential factor given in (4.4) was used to estimate the collision efficiency coefficient in the large total strain limit. These power laws suggest that the simulated coagulation rate should remain relatively constant or decrease slightly from moderate to large total strains. For small total strain the coagulation rate should decrease because the coagulation rate constant depends on a positive power of the total strain. The effect of simultaneously varying $\tau_S \Gamma_\eta$ and $\tau_R \Gamma_\eta$ is shown in figure 9. The results are for 3.8 μm diameter polystyrene particle ($N_L = 237$) in turbulent flows with shear rates of 28 s^{-1} ($N_S = 1761$) and 280 s^{-1} ($N_S = 17610$). The symbols represent the simulation data for $\Gamma_\eta = 28$ s^{-1} (squares), and $\Gamma_\eta = 280$ s^{-1} (circles). Comparing figures 9 and 4 shows that at small total strain k has the same trend as k^0; an increase in the normalized coagulation rate constant is seen with increasing total strain up to $\tau_S \Gamma_\eta \sim 1$. Beyond $\tau_S \Gamma_\eta \sim 1$ the normalized coagulation rate constant goes through a minimum at $\tau_S \Gamma_\eta \sim 5$. Differences in coagulation rate constant calculations at total strains of 1 and 5 are statistically significant (z-test, $p = 0.026$ when $N_S = 1761$ and $p = 0.003$ when $N_S = 17610$). Within the statistical uncertainty of the data, the normalized rate constant remains unchanged as the total strain increases above $\tau_S \Gamma_\eta \sim 5$; however, the fact that both data sets show the normalized rate constant increasing again for total strains above 5 does lend some credence to the trend. The relative drop in the coagulation rate constant when going from $\tau_S \Gamma_\eta$ of 1 to 5 can be used to estimate the
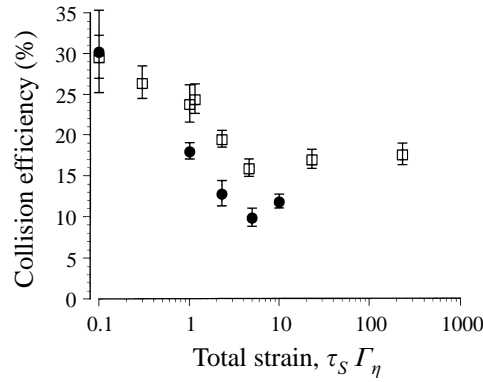
FIGURE 10. The effect of simultaneously varying $\tau_S \Gamma_\eta$ and $\tau_R \Gamma_\eta$ on the collision efficiency for 1.9 μm radius particles when $\square$, $N_S = 1761$; $\bullet$, $N_S = 17610$. The error bars are $\pm$ one standard deviation from the mean and the ratio of total rotation to total strain is held fixed at 3.13.

Kolmogorov shear rate power law expected in the large total strain limit. In the absence of interparticle interactions, the normalized rate constants differ slightly (compare $k^0 = 8.62$ for isotropic turbulence and $k^0 = 9.96$ in the large total strain and large total rotation limit). Assuming the pre-exponential factors for interacting particles at moderate and large total strain are similar, the two data sets in figure 9 suggest that $k \sim \Gamma_\eta^{0.78}$ at large total strain. This dependence on the shear rate is more closely aligned to the prediction for simple shear than with uniaxial extension (Feke & Schowalter 1983). The apparent correspondence between the large total strain limit and the simple shear rates might have been expected. In both simple shear and turbulence, the shear rate partitions equally between rotational and extension components. The importance of rotation has been demonstrated to decrease the coagulation rate in both the random flow discussed in this manuscript and steady linear flows (Greene *et al.* 1994).

The collision efficiency, $\alpha = k/k^0$, calculated from the data presented in figure 9 is shown in figure 10. α varies between 16 and 30 % for the $\Gamma_\eta = 28 \text{ s}^{-1}$ computations (squares) and between 10 and 30 % for the $\Gamma_\eta = 280 \text{ s}^{-1}$ simulations. In both cases, the small total strain calculations show the largest collision efficiencies. In the small total strain limit the collision efficiency varies as $\alpha \approx (\tau_S \Gamma_\eta)^{-1/2} N_S^{-1/2}$, which increases as the total strain decreases. The reason coagulation at small total strain is more efficient may be explained by considering the relative motion of two particles in the large and small total strain limits. Neglecting the influence of closed streamlines, at large total strain, interacting particles have essentially one opportunity to interact and collide before the persistent flow field sweeps them away from each other. In the diffusive limit, particle trajectories are random and a pair of particles will have multiple encounters before they separate. Thus each particle pair is given several chances to collide in the small strain limit and that increases the probability that the two particles will have a successful collision.

5. Conclusion

The objectives of this study were threefold: (i) to develop a simulation method, valid at arbitrary total strain and rotation, that could be used to compute the trajectories of coagulating particles with radii smaller than the Kolmogorov length of turbulence; (ii)

to compare the coagulation rate constant for non-interacting particles at arbitrary total strain to the asymptotic limits of large and small strain derived previously (Saffman & Turner 1956; Brunk *et al.* 1997); and (iii) to compute the effect of particle interactions on coagulation in isotropic turbulence.

The relative motion of a particle pair was simulated by solving an equation of motion valid for particles with diameters smaller than the Kolmogorov lengthscale. The velocity field was assumed to be a randomly varying, locally linear flow field. We expanded the velocity gradient as a temporal Fourier series with components constrained to reproduce the two-time Lagrangian statistics of the fluctuating turbulent velocity gradient tensor. Coagulation rates were computed for non-interacting particles and interacting particles affected by van der Waals attraction.

Resulting simulations for the non-interacting particles indicate that both large and small total strain asymptotes overestimate the actual coagulation rate. A hyperbolic interpolation of the asymptotic limits reproduces the numerical calculation to within 5% of the actual values; thus, by knowing the asymptotic forms in the diffusion (Brunk *et al.* 1997) and pseudostationary limits, the behaviour in the intermediate regime can be estimated over the range of strain rate correlation times.

Although our primary emphasis was on coagulation in turbulent flow, we have also considered the coagulation rate in a range of isotropic Gaussian random flow fields with correlation times differing from those in turbulence. By varying the flow correlation time, we show how the kinematics of the flow can influence coagulation and place this study in the wider context of coagulation in randomly fluctuating flows. Randomly fluctuating flows may also arise in porous media (Shaqfeh & Koch 1992) or in chaotic flows (for example, Ottino 1991; Muzzio & Ottino 1988). While these flows are generally not isotropic, the dependence of coagulation on strain and rotation may show similar trends.

We found that the total rotation (product of the rotation rate and the rotation rate correlation time) affects the particle collision rate. We believe this to be the first time the role of rotation has been systematically investigated. Indeed, we find that Saffman & Turner's (1956) analysis, valid in the large total strain limit, neglects rotation and overpredicts the turbulent coagulation simulations by about 5%. Rotation is shown here to decrease the observed coagulation rate at large total strain and the absence of rotation in the Saffman & Turner model explains the discrepancy with these computer simulations. The presence of rotation leads to recirculating streamlines in the flow. Since coagulation is limited to open streamlines that can bring particles from the bulk, the presence of curved streamlines that leave and return to the excluded volume surface decreases the coagulation rate. Additional investigations into the separate effects of the strain and rotation rate correlation times show that the coagulation rate decreases as the rotation rate correlation time increases. This decrease results from persistent recirculating streamlines that form in the system at large total rotation. At small $\Gamma_\eta \tau_R$, rotation does not effect the coagulation rate because there is some probability that as the velocity field evolves, a particle on a streamline that returns to the excluded volume surface of the test sphere can escape the looped trajectory before returning to $r = \sigma$.

The consideration of hydrodynamic interactions and retarded van der Waals attractions leads to significant decreases in the computed coagulation rate constant. For instance, a 4 μm diameter particle experiencing $\Gamma_\eta = 10 \text{ s}^{-1}$ has a collision efficiency, α, of about 20%. In other words, only one collision between interacting particles occurs for every five that occur in the absence of interparticle interactions. For a given particle size an optimal shear rate that leads to a maximum coagulation efficiency exists. At the maximum collision efficiency, the turbulent shear is just strong

enough to bring the particle pair to gap widths at which van der Waals forces can take over and cause a collision. For larger shear rates, the turbulence drives the particles to small gap widths before the van der Waals attraction is sufficient to cause a collision. Since lubrication forces increase with decreasing gap width, the large shear rates experience a larger resistance to collision and the transport efficiency of the turbulence declines. For weak turbulence, the shear is not strong enough to transport particles to gap widths where van der Waals forces are significant and therefore the collision efficiency is lower. A simple balance based on the turbulent particle flux and the flux due to the van der Waals attractive forces predicts the location of the maximum collision efficiency.

Simulations performed at a constant shear number (i.e. ratio of viscous to van der Waals forces) and various values of the total strain show that order one total strains have the highest coagulation rate. Two competing effects lead to this result: the transport rate of the flow field and the probability that two interacting particles will collide before the flow field transports them away from each other. The rate of transport toward the test sphere increases with total strain as the transport mechanism changes from diffusive transport at small total strain to transport in a pseudosteady flow field at large total strain. The higher rates of transport found at large total strains increase the coagulation rate constant because more particles are available for coagulation. Working against this process is the efficiency of the particle encounters. In simplest terms, at large total strain, approaching particles have essentially one opportunity for successful collision before the persistent flow field carries them away from each other. In contrast, in the diffusive limit of small total strain, particle positions fluctuate randomly so that approaching particles will undergo many close encounters before they either collide or are transported away from each other. The many opportunities for collision available in the diffusion limit increase the probability that the particles will actually collide, so the efficiency of the process is higher than at large total strain. The synergistic combination of relatively efficient particle transport and multiple particle encounters that occurs for total strains of order one explains why flows with moderate total strain have the highest coagulation rate.

There are several recent studies of particle collision rates in turbulent flow fields obtained from direct numerical simulations (Sundaram & Collins 1997; Wang *et al.* 998; Zhou *et al.* 1998). In each case, the particles were assumed not to influence the turbulent flow. Sundaram & Collins (1997) and Zhou *et al.* (1998) considered particles with finite Stokes numbers, while Wang *et al.* (1998) considered inertialess particles. Many of the results of Wang *et al.* and Zhou *et al.* are for frozen turbulence although a few calculations with temporally evolving turbulence were also included. The primary advantage of DNS is that it provides an exact representation of the turbulent field. However, it is difficult to provide a realistic description of a dilute suspension of colloidal-sized interacting particles within the context of DNS. The colloidal and hydrodynamic interparticle interactions occur on very short timescales and lengthscales which are difficult to resolve at the same time as one is resolving the larger scales. For this reason, all of the studies mentioned above neglected particle interactions.

It is also difficult to simulate particles with diameters that are much smaller than the Kolmogorov scale in DNS. The collision rate decreases with decreasing particle diameter and it is difficult to obtain a statistically significant number of collisions for $\sigma \quad \eta$. Sundaram & Collins (1997) found that σ must be at least as small as 0.18η to obtain the small-particle behaviour for particles with a constant Stokes number, $St = 1$. Wang *et al.*'s (1998) simulations used a surprisingly large particle diameter: $\sigma > 0.8\eta$.

The need to obtain a sufficiently large number of collisions to obtain statistically significant results led the DNS investigators to use moderate values of the volume fraction, typically $\phi = O(0.01)$. As noted in §1, the volume fraction must be quite small to avoid concentration fluctuations from developing because the mixing time becomes comparable with the time for the volume fraction to evolve owing to coagulation. Written in terms of the Taylor-scale Reynolds number, we require $\phi \lesssim R_\lambda^{-3/2}$. Since R_λ is typically 25–55 in the simulations, one would require $\phi \lesssim 0.01$ to avoid concentration fluctuations over the integral scales of the turbulence.

Sundaram & Collins (1997) assumed elastic interparticle collisions upon contact. This collision mechanism does not introduce concentration fluctuations because particles are conserved by the collision. However, as noted by the authors, elastic collisions give physically unrealistic behaviour at small Stokes numbers especially in the absence of hydrodynamic interactions where two particles might collide repeatedly.

Wang *et al.* (1998) removed pairs of particles from the simulation whenever they came into contact to model the coagulation event. They thereby either obtained a number density that decreased with time as the simulation progressed (their scheme 3) or added particles at random throughout the flow to keep the number density constant (their scheme 4). Wang *et al.* (1998) noted that number density variations developed during the flow because particles were removed more rapidly from regions of high dissipation. They also noted that schemes 3 and 4 yielded different apparent coagulation rates. These results are not surprising since the volume fractions $\phi = 0.002$ to 0.12 used in these simulations do not satisfy the criterion for a well-mixed suspension. Thus, these simulations cannot be directly compared with our calculations or those of Saffman & Turner (1956) without a model for the macroscale mixing phenomena. The clearest comparison of DNS with theory would be obtained if it were possible to simulate smaller particle volume fractions where mixing effects would be absent. In addition, it would be desirable to vary the volume fraction and particle radius independently.

In §3, we noted that even in the limit of large total strain, the coagulation rate is smaller than that predicted by Saffman & Turner (1956) by about 5% owing to the effects of rotation. The rotational component of the flow leads to some trajectories that leave the excluded volume region and then return again. These should not be counted toward the coagulation rate, since the concentration of singlets is zero at $r = \sigma$. Allowing for the finite-strain amplitude of a real turbulent flow, we found the coagulation rate to be 20% lower than Saffman & Turner (1956). Wang *et al.* (1998) performed some simulations (their scheme 1) in which the particle pairs were allowed to overlap and were not removed from the calculation. These simulations reproduced the results of Saffman & Turner (1956) for the coagulation rate. These simulations counted as coagulation events in which overlapping particle pairs passed out of and then back into the excluded volume region. Thus, scheme 1 of Wang *et al.* (1988) did not detect the decreased coagulation rate owing to closed trajectories.

These first attempts at simulating turbulent coagulation in DNS illustrate the need to recognize, control and evaluate the effects of particle size, volume fraction, flow evolution timescales and interparticle interactions in future computations. The DNS studies discussed above provide evidence that some of these effects can be significant; however, systematic studies are needed to understand each effect independently. Our work has documented the effects of flow evolution time and interparticle forces on rates of aggregation in turbulence.

The simulations conducted in this research are an important step in improving the understanding of colloidal aggregation in turbulence. What remains is to obtain

accurate experimental measurements of turbulent coagulation for comparison to the model predictions. As a next phase in this research turbulent coagulation rates for monodisperse particles will be measured under conditions of isotropic turbulence created by an oscillating grid reactor (Brunk *et al.* 1998).

Appendix. The second-order statistics of $\Gamma_{ij}(t)$

We assume an isotropic fluctuating velocity gradient characterized by separate strain and rotation rate correlation times. Mean flow is ignored so that the expectation of $\Gamma_{ij}(t)$ is zero. The velocity gradient tensor is separated into its symmetric and antisymmetric parts so that the strain and rotation rates are decoupled along with their timescales:

$$\Gamma_{ij}(t) = S_{ij}(t) + R_{ij}(t), \tag{A 1}$$

where $S_{ij}(t)$ is the strain rate tensor and $R_{ij}(t)$ is the rotation rate tensor.

In the following analysis all times and velocity gradients have been scaled with their Kolmogorov values. Assuming stationary turbulence, the two-time correlation for $\Gamma_{ij}(t)$ is written as:

$$\langle \Gamma_{ik}(0)\, \Gamma_{jl}(t) \rangle = \langle S_{ik}(0)\, S_{jl}(t) \rangle + \langle R_{ik}(0)\, R_{il}(t) \rangle, \tag{A 2}$$

where the cross-correlation terms, such as $\langle S_{ik}(0)\, R_{jl}(t) \rangle$, are zero owing to isotropy; however, correlations would occur for the third moments if we considered non-Gaussian velocity gradient fields. Angle brackets, $\langle \ \rangle$, denote ensemble averaging over the sample space of the random variable.

Velocity gradient autocorrelation data obtained from DNS (Girimaji & Pope 1990) and the properties of isotropic fourth-order tensors are used to deduce relationships for the strain and rotation rate autocorrelation functions. The strain correlation function decays exponentially with a characteristic decay time, τ_S, of $2.3\tau_\eta$ (Girimaji & Pope 1990):

$$\langle S_{ik}(0)\, S_{jl}(t) \rangle = S_{ikjl} \exp\!\left(\frac{-t}{\tau_S}\right), \tag{A 3}$$

where the fourth-order tensor S_{ikjl} is the covariance of the strain rate. Nonlinear regression of Girimaji & Pope's simulation data (1990) shows that the exponential form given in (A 3) fits the data with an $r^2 = 99.6\%$. S_{ikjl} is written as a fourth-order isotropic tensor that depends on three scalar coefficients. The numerical coefficients are obtained by applying symmetry, $S_{ikjl} = S_{kijl}$, continuity, $S_{iijl} = S_{ikjj} = 0$, and dissipation rate, $S_{ijij} = 0.5$. The final form for the strain rate covariance is:

$$S_{ikjl} = \tfrac{1}{20}[\delta_{ij}\,\delta_{kl} + \delta_{il}\,\delta_{jk} - \tfrac{2}{3}\delta_{ik}\,\delta_{jl}]. \tag{A 4}$$

The rotation rate correlation function is obtained using a similar analysis to yield:

$$\langle R_{ik}(0)\, R_{jl}(t) \rangle = R_{ikjl} \exp\!\left(\frac{-t}{\tau_R}\right), \tag{A 5}$$

where
$$R_{ikjl} = \tfrac{1}{12}[\delta_{ij}\,\delta_{kl} - \delta_{il}\,\delta_{jk}], \tag{A 6}$$

and τ_R is the rotation rate correlation time with a value estimated to be about $7.2\tau_\eta$ (Girimaji & Pope 1990). The exponential form for the autocorrelation function fits the DNS data with $r^2 = 95\%$. The form of (A 6) is set by applying antisymmetry $R_{ikjl} = -R_{kijl}$, continuity, $R_{iijl} = R_{ikjj} = 0$, and dissipation rate, $R_{ijij} = 0.5$. The last statement comes from the evolution equation for the mean square vorticity fluctuations and is valid for large Reynolds numbers (Tennekes & Lumley 1972).

The complete expression for the autocorrelation function of the velocity gradient tensor is:

$$\langle \Gamma_{ik}(0)\,\Gamma_{jl}(t)\rangle = S_{ikjl}\exp\!\left(\frac{-t}{\tau_S}\right) + R_{ikjl}\exp\!\left(\frac{-t}{\tau_R}\right). \tag{A 7}$$

REFERENCES

ADLER, P. M. 1981 Heterocoagulation in shear flow. *J. Colloid. Interface Sci.* **83**, 106–115.

BATCHELOR, G. K. & GREEN, J. T. 1972a The hydrodynamic interaction of two small freely-moving spheres in a linear flow field. *J. Fluid Mech.* **56**, 375–400.

BATCHELOR, G. K. & GREEN, J. T. 1972b The determination of the bulk stress in a suspension of spherical particles to order c^2. *J. Fluid Mech.* **56**, 401–427.

BATCHELOR, G. K. 1976 Brownian diffusion of particles with hydrodynamic interaction. *J. Fluid Mech.* **74**, 1–29.

BROWN, B. W. & LOVATO, J. 1996 *RANLIB.C: Library of C Routines for Random Number Generation.* NETLIB, NETLIB. ATT.COM.

BRUNK, B. K., KOCH, D. L. & LION, L. W. 1997 Hydrodynamic pair diffusion in isotropic random velocity fields with application to turbulent coagulation. *Phys. Fluids.* **9**, 2670–2691.

BRUNK, B. K., KOCH, D. L. & LION, L. W. 1998 Observations of coagulation in isotropic turbulence. *J. Fluid Mech.* (submitted).

CAMP, T. R. & STEIN, P. C. 1943 Velocity gradients and internal work in fluid motion. *J. Bost. Soc. Civil Engng* **30**(4), 219–237.

CASSON, L. W. & LAWLER, D. F. 1990 Flocculation in turbulent flow: measurement and modeling of particle size distributions. *AWWA J.* **8**, 54–68.

DAVIS, R. H. 1984 The rate of coagulation of a dilute polydisperse system of sedimenting spheres. *J. Fluid Mech.* **145**, 179–199.

DELICHATSIOS, M. A. & PROBSTEIN, R. F. 1975 Coagulation in turbulent flow: theory and experiment. *J. Colloid Interface Sci.* **51**, 394–405.

FEKE, D. L. & SCHOWALTER, W. R. 1983 The effect of Brownian diffusion on shear-induced coagulation of colloidal dispersions. *J. Fluid Mech.* **133**, 17–35.

GIRIMAJI, S. S. & POPE, S. B. 1990 A diffusion model for velocity gradients in turbulence. *Phys. Fluids* A **2**, 242–256.

GREENE, M. R., HAMMER, D. A. & OLBRICHT, W. L. 1994 The effect of hydrodynamic flow field on colloidal stability. *J. Colloid Interface Sci.* **167**, 232–246.

ISRAELACHVILI, J. 1992 *Intermolecular and Surface Forces*, 2nd edn. Academic.

KIM, S. & KARRILA, S. J. 1991 *Microhydrodynamics: Principles and Selected Applications,* chap. 7, 11. Butterworth–Heinemann.

KRAICHNAN, R H. 1970 Diffusion by a random velocity field. *Phys. Fluids* **13**, 22–31.

KRONE, R. B. 1978 *Estuarine Transport Processes* (ed. B. Kferfve). University of South Carolina Press.

LEVICH, V. G. 1962 *Physiochemical Hydrodynamics*, pp. 139–231. Prentice-Hall.

McCAVE, I. N. 1984 Size spectra and aggregation of suspended particles in the deep ocean. *Deep-Sea Res.* **31**, 329–352.

MUZZIO, F. J. & OTTINO, J. M. 1988 Coagulation in chaotic flows. *Phys. Rev.* A **38**, 2516–2524.

O'MELIA, C. R. 1980 Aquasols: the behavior of small particles in aquatic systems. *Environ. Sci. Technol.* **14**, 1052–1060.

OTTINO, J. M. 1991 Unity and diversity in mixing: stretching, diffusion, breakup, and aggregation in chaotic flows. *Phys. Fluids* A **3**, 1417–1430.

PEARSON, H. J., VALIOULIS, I. A. & LIST, E. J. 1984 Monte Carlo simulation of coagulation in discrete particle-size distributions. Part 1. Brownian motion and fluid shearing. *J. Fluid Mech.* **143**, 367–385.

POPE, S. B. 1990 Lagrangian microscales of turbulence. *Phil. Trans. R. Soc. Lond.* A **333**, 309–319.

POPE, S. B. 1996 *Turbulent Flows*, chap. 1–7, §6.7.2.

RUSSEL, W. B., SAVILLE, D. A. & SCHOWALTER, W. R. 1989 *Colloidal Dispersions*. Cambridge University Press.

SAFFMAN, P. G. & TURNER, J. S. 1956 On the collision of drops in turbulent clouds. *J. Fluid Mech.* **1**, 16–30.

SCHENKEL, J. H. & KITCHENER, J. A. 1960 At test of the Derjaguin–Verwey–Overbeek theory with a colloidal suspension. *Trans. Faraday Soc.* **56**, 161–173.

SHAQFEH, E. S. G. & KOCH, D. L. 1992 Polymer stretch in dilute fixed beds of fibres or spheres. *J. Fluid Mech.* **244**, 17–54.

SQUIRES, K. D. & EATON, J. K. 1991 Particle response and turbulence modification in isotropic turbulence. *Phys. Fluids* A **2**, 1191–1203.

STUMM, W. & MORGAN, J. J. 1981 *Aquatic Chemistry: An Introduction Emphasizing Chemical Equilibrium in Natural Waters*, §10.7. Wiley.

SUNDARAM, S. & COLLINS, L. R. 1997 Collision statistics in an isotropic particle-laden turbulent suspension. Part 1. Direct numerical simulations. *J. Fluid Mech.* **335**, 75–109.

SURESH, L. & WALZ, J. Y. 1996 Effect of surface roughness on the interaction energy between a colloidal sphere and a flat plate. *J. Colloid Interface Sci.* **183**, 199–213.

TENNEKES, H. & LUMLEY, J. L. 1972 *A First Course in Turbulence*. MIT Press.

TOWNSEND, A. A. 1951 The diffusion of heat spots in isotropic turbulence. *Proc. R. Soc. Lond.* A **209**, 418–430.

VAN DE VEN, T. G. M. & MASON, S. G. 1977 The microrheology of colloidal dispersions. VII. Orthokinetic double formation of spheres. *Colloid Polymer Sci.* **255**, 468–479.

VON NEUMANN, J. 1951 Various techniques used in connection with random digits. *US Natl Bur. Stands. Appl. Math. Ser.* **12**, 36.

WANG, L. & MAXEY, M. R. 1993 Settling velocity and concentration distribution of heavy particles in homogeneous isotropic turbulence. *J. Fluid Mech.* **256**, 27–68.

WANG, L.-P., WEXLER, A. S. & ZHOU, Y. 1998 On the collision rate of small particles in isotropic turbulence. Part 1. Zero-inertia case. *Phys. Fluids* **10**, 266–276.

YEUNG, P. K. & POPE, S. B. 1989 Lagrangian statistics from direct numerical simulations of isotropic turbulence. *J. Fluid Mech.* **207**, 531–586.

ZEICHNER, G. R. & SCHOWALTER, W. R. 1977 Use of trajectory analysis to study stability of colloidal dispersions in flow fields. *AIChE J.* **23**, 243–254.

ZHOU, Y., WEXLER, A. S. & WANG, L.-P. 1998 On the collision rate of small particles in isotropic turbulence. Part 2. Finite inertia case. *Phys. Fluids* (submitted).